Exploring the sensitivity to non-standard and generalized neutrino interactions through coherent elastic neutrino-nucleus scattering with a NaI detector

Sabya Sachi Chatterjee,[1,2,*] Stéphane Lavignac,[2,†] O. G. Miranda,[3,‡] and G. Sanchez Garcia[4,§]

[1] *Institut für Astroteilchenphysik, Karlsruher Institut für Technologie (KIT), 76131 Karlsruhe, Germany*

[2] *Institut de Physique Théorique, Université Paris Saclay, CNRS, CEA, F-91191 Gif-sur-Yvette, France*

[3] *Departamento de Física, Centro de Investigación y de Estudios Avanzados del IPN, Apartado Postal 14-740 07000, Ciudad de Mexico, Mexico*

[4] *Instituto de Física Corpuscular (CSIC-Universitat de València), Parc Científic UV, C/ Catedràtico José Beltrán, 2, 46980 Paterna, Spain*

After the first observation of coherent elastic neutrino-nucleus scattering (CEνNS) by the COHERENT collaboration, many efforts are being made to improve the measurement of this process, making it possible to constrain new physics in the neutrino sector. In this paper, we study the sensitivity to non-standard interactions (NSIs) and generalized neutrino interactions (GNIs) of a NaI detector with characteristics similar to the one that is currently being deployed at the Spallation Neutron Source at Oak Ridge National Laboratory. We show that such a detector, whose target nuclei have significantly different proton to neutron ratios (at variance with the current CsI detector), could help to partially break the parameter degeneracies arising from the interference between the Standard Model and NSI contributions to the CEνNS cross section, as well as between different NSI parameters. By contrast, only a slight improvement over the current CsI constraints is expected for parameters that do not interfere with the SM contribution. We find that a significant reduction of the background level would make the NaI detector considered in this paper very efficient at breaking degeneracies among NSI parameters.

I. INTRODUCTION

Coherent elastic neutrino-nucleus scattering (CEνNS) [1] is a privileged process to probe new physics in the neutrino sector. So far, the only measurements of CEνNS have been done at the Spallation Neutron Source (SNS) at Oak Ridge National Laboratory, USA, by the COHERENT collaboration. The first observation of this process was performed with a CsI detector [2, 3]. Another detector, with liquid Argon as a target, was subsequently used by the COHERENT collaboration [4].

* sabya.chatterjee@kit.edu
† stephane.lavignac@ipht.fr
‡ omar.miranda@cinvestav.mx
§ gsanchez@fis.cinvestav.mx

These measurements allowed to test the Standard Model at low energy [5], to constrain the neutron root mean square *(rms)* radius of Cesium, Iodine [6] and Argon [7], and to probe various possible manifestations of physics beyond the Standard Model, such as non-standard neutrino interactions (NSIs) [8–11], generalized neutrino interactions (GNIs) [10, 12–14], neutrino electromagnetic properties [15–17], new light gauge bosons [13, 18–20] and sterile neutrinos [10, 21, 22], among others. Future CEνNS experiments at spallation neutron sources [23–25] or nuclear reactors [26–29] will provide more data using different target materials. Particularly interesting is the possibility to disentangle new physics from Standard Model parameters using the interplay between experiments with different neutrino sources [30, 31]. In addition, using nuclear targets with different proportions of protons and neutrons can help reduce the parameter degeneracies arising from the interference between standard and non-standard contributions to CEνNS, e.g., in the presence of NSIs [8].

A broad class of new physics models predict low-energy effects in the lepton sector that can effectively be described in terms of NSIs or GNIs [32–35]. CEνNS is an excellent process to test such new physics effects and to resolve the degeneracies that appear in the interpretation of neutrino oscillation data in the presence of NSIs [36, 37]. However, the possibility of constraining NSI parameters with CEνNS is limited by the possible cancellations between standard and non-standard contributions to the cross section, as well as between different NSI couplings. It is, therefore, crucial to perform CEνNS measurements with different neutrino sources and targets in order to break these degeneracies [8, 9, 24, 37–39].

In this work, we study the expected sensitivity to non-standard and generalized neutrino interactions of a NaI detector with characteristics similar to the one that is currently being deployed at the SNS. NaI, as opposed to CsI, has the important feature of consisting of two target nuclei with significantly different proton-to-neutron ratios ($p/n \simeq 0.72$ for Iodine and $p/n \simeq 0.92$ for Sodium). We show that this property of the NaI detector makes it particularly efficient at reducing the degeneracies between NSI parameters, provided that the signal-over-background ratio is sufficiently large. For generalized neutrino interactions and off-diagonal NSIs, no significant improvement over the constraints extracted from the current CsI data is expected, unless the signal systematic uncertainty can be reduced below 10%.

The paper is structured as follows. In Section II, we discuss the NSI and GNI contributions to the CEνNS cross section. In Section III, we present the experimental setup at the SNS and the characteristics of the current CsI and future NaI detectors. Section IV details our analysis procedure. The expected sensivities of the future NaI detector to NSI and GNI parameters are presented in Section V, and compared with the current CsI constraints. The impact of the statistics, signal

systematic uncertainty and background level are also studied in this section. Finally, we present our conclusions in Section VI.

II. THEORETICAL FRAMEWORK

In this section, we discuss the tools needed to probe GNIs through CEνNS measurements. We begin by introducing the SM prediction for the CEνNS cross section, then we discuss how this cross section is modified when GNI parameters are introduced.

A. The standard CEνNS cross section

In the Standard Model, the cross section for the coherent elastic scattering of a neutrino or antineutrino of flavor α ($\alpha = e, \mu, \tau$) and energy E_ν off a nucleus with Z protons, N neutrons and mass M is given (up to subleading terms of order T/E_ν, $(T/E_\nu)^2$ [8] and small radiative corrections [40]) by [1]

$$\frac{\mathrm{d}\sigma}{\mathrm{d}T}(E_\nu, T) \;=\; \frac{G_F^2 M}{\pi}\left(1 - \frac{MT}{2E_\nu^2}\right) F^2(|\vec{q}|^2)\, Q_{W,\alpha}^2 \;, \tag{1}$$

where G_F is the Fermi constant, T the nuclear recoil energy, $F(|\vec{q}|^2)$ the form factor of the nucleon distribution in the nucleus [41] (assumed to be the same for protons and neutrons) evaluated at the transferred three-momentum $|\vec{q}| \simeq \sqrt{2MT}$, and

$$Q_{W,\alpha} \;=\; Z g_V^p + N g_V^n \,, \tag{2}$$

with $g_V^p = \frac{1}{2} - 2\sin^2\theta_W$ and $g_V^n = -\frac{1}{2}$, is the weak nuclear charge. Since $|\vec{q}|$ is typically very small in CEνNS, the value of the weak mixing angle is taken at zero momentum transfer ($\sin^2\theta_W = 0.23867$ [42, 43]).

The form factor $F(|\vec{q}|^2)$ describe the loss of coherence of the scattering when $|\vec{q}| \gtrsim R^{-1}$, where R is the nucleon radius. Following the COHERENT collaboration, we use the Klein-Nystrand parametrization for the nuclear form factor [44],

$$F(|\vec{q}|^2) \;=\; 3\,\frac{j_1(|\vec{q}|R_A)}{|\vec{q}|R_A}\left(\frac{1}{1 + |\vec{q}|^2 a_k^2}\right) \,, \tag{3}$$

where $j_1(x) = (\sin x - x\cos x)/x^2$ is the spherical Bessel function of order one, $a_k = 0.9\,\mathrm{fm}$ and $R_A = 1.23A^{1/3}\,\mathrm{fm}$ is the nuclear radius, with A the total number of nucleons of the target nucleus.

B. Non-standard and generalized neutrino interactions

The CEνNS cross section is potentially affected by any interaction between neutrinos and quarks that may be generated by new physics beyond the Standard Model. The simplest example of such interactions are the so-called (neutral-current) non-standard neutrino interactions (NC-NSIs, or NSIs for short), whose phenomenology has been widely studied [33–35, 45]. They are usually parametrized as

$$\mathcal{L}_{\text{NC-NSI}} \;=\; -\sqrt{2}\,G_F \left\{ \varepsilon^{fV}_{\alpha\beta} \left(\overline{\nu}_\alpha \gamma^\mu P_L \nu_\beta\right)\left(\overline{f}\gamma_\mu f\right) + \varepsilon^{fA}_{\alpha\beta} \left(\overline{\nu}_\alpha \gamma^\mu P_L \nu_\beta\right)\left(\overline{f}\gamma_\mu \gamma^5 f\right) \right\}, \tag{4}$$

where $\alpha, \beta = e, \mu, \tau$ denote the neutrino flavors, $f = u, d$ label the up and down quarks (we omit the leptonic NSIs, $f = e$, as they do not contribute to CEνNS), summation over α, β and f is implicit, and $\varepsilon^{fV}_{\alpha\beta}$, $\varepsilon^{fA}_{\alpha\beta}$ are the vector and axial-vector NSI couplings, respectively. In this paper, we do not consider the axial-vector NSIs, because their contribution to the CEνNS cross section depends on the nuclear spin and is therefore negligible for heavy nuclei [12], similarly to the contribution of the neutral current axial couplings in the SM [8, 46].

Non-standard neutrino-quark interactions can have a more general Lorentz structure than the one of Eq. (4). Namely, one may also consider scalar, pseudo-scalar and tensor couplings[1], usually dubbed "generalized neutrino interactions" (GNIs) in the literature [12, 32, 48]

$$\begin{aligned} \mathcal{L}_{\text{GNI}} \;=\; -\sqrt{2}\,G_F \quad & \left\{ \varepsilon^{qS}_{\alpha\beta} \left(\overline{\nu}_\alpha P_L \nu_\beta\right)\left(\overline{q} q\right) + \varepsilon^{qP}_{\alpha\beta} \left(\overline{\nu}_\alpha P_L \nu_\beta\right)\left(\overline{q}\gamma^5 q\right) \right. \\ & \left. + \varepsilon^{qT}_{\alpha\beta} \left(\overline{\nu}_\alpha \sigma^{\mu\nu} P_L \nu_\beta\right)\left(\overline{q}\sigma_{\mu\nu} P_L q\right) \right\} + \text{h.c.}\,, \end{aligned} \tag{5}$$

where $\sigma^{\mu\nu} = \frac{i}{2}\left[\gamma^\mu, \gamma^\nu\right]$ and $q = u, d$. Generally, NSIs are also included in the GNI Lagrangian. In the following, we will refer to $\varepsilon^{qS}_{\alpha\beta}$, $\varepsilon^{qV}_{\alpha\beta}$ and $\varepsilon^{qT}_{\alpha\beta}$ as scalar, vector and tensor couplings, respectively (we will not consider pseudo-scalar interactions, which give a negligible contribution to CEνNS [12, 32]). Note that hermiticity of the Lagrangian implies $\varepsilon^{qV}_{\beta\alpha} = \left(\varepsilon^{qV}_{\alpha\beta}\right)^*$, while the matrices of scalar and tensor couplings do not have any particular symmetry property if neutrinos are Dirac fermions. If they are Majorana fermions, instead, one has $\varepsilon^{qS}_{\beta\alpha} = \varepsilon^{qS}_{\alpha\beta}$ and $\varepsilon^{qT}_{\beta\alpha} = -\varepsilon^{qT}_{\alpha\beta}$ (in particular, flavor-diagonal tensor couplings vanish for Majorana neutrinos).

In the presence of scalar, vector and tensor non-standard neutrino interactions, the differential CEνNS cross section (1) for an incident neutrino of flavor α is modified to [32]

$$\begin{aligned} \frac{\mathrm{d}\sigma}{\mathrm{d}T}(E_\nu, T) \;=\; \frac{G_F^2 M}{\pi}\, F^2(|\vec{q}|^2) \sum_{\beta\,=\,e,\,\mu,\,\tau} & \left[\left|C^S_{\beta\alpha}\right|^2 \frac{MT}{8E_\nu^2} + \left|C^V_{\beta\alpha} + Q_{W,\alpha}\,\delta_{\alpha\beta})\right|^2 \left(1 - \frac{MT}{2E_\nu^2}\right) \right. \\ & \left. + 2\left|C^T_{\beta\alpha}\right|^2 \left(1 - \frac{MT}{4E_\nu^2}\right) \right], \end{aligned} \tag{6}$$

[1] The tensor operators $\left(\overline{\nu}_\alpha \sigma^{\mu\nu} P_L \nu_\beta\right)\left(\overline{q}\sigma_{\mu\nu} P_R q\right)$ vanish by Lorentz symmetry [47], hence do not appear in Eq. (5).

where subleading terms of order $T/E_\nu \ll MT/E_\nu^2$ have been omitted[2]. For an incident antineutrino of flavor α, one should replace $C^S_{\beta\alpha} \to C^S_{\alpha\beta}$, $C^V_{\beta\alpha} \to C^V_{\alpha\beta}$ and $C^T_{\beta\alpha} \to C^T_{\alpha\beta}$ in Eq. (6). The SM contribution is contained in the weak nuclear charge $Q_{W,\alpha}$, given by Eq. (2), while the non-standar contributions are encapsulated in the coefficients $C^S_{\alpha\beta}$, $C^V_{\alpha\beta}$ and $C^T_{\alpha\beta}$, which are given by [12]

$$C^S_{\alpha\beta} = \sum_{q=u,d} \left(Z \frac{m_p}{m_q} f_q^p + N \frac{m_n}{m_q} f_q^n \right) \varepsilon^{qS}_{\alpha\beta} \,, \tag{7}$$

$$C^V_{\alpha\beta} = (2Z + N)\, \varepsilon^{uV}_{\alpha\beta} + (Z + 2N)\, \varepsilon^{dV}_{\alpha\beta} \,, \tag{8}$$

$$C^T_{\alpha\beta} = \sum_{q=u,d} \left(Z\delta_q^p + N\delta_q^n \right) \varepsilon^{qT}_{\alpha\beta} \,, \tag{9}$$

For the numerical coefficients appearing in Eqs. (7) and (9), we adopt the values given in Refs. [49] and [50], respectively:

$$f_u^p = 0.0208 \,, \quad f_d^p = 0.0411 \,, \quad f_u^n = 0.0189 \,, \quad f_d^n = 0.0451 \,, \tag{10}$$

$$\delta_u^p = 0.792 \,, \quad \delta_d^p = -0.194 \,, \quad \delta_u^n = -0.194 \,, \quad \delta_d^n = \ 0.792 \,. \tag{11}$$

As for quark masses, we use the central values given by the Particle Data Group [43], $m_u = 2.2\,\text{MeV}$ and $m_d = 4.7\,\text{MeV}$. Given the large uncertainties associated with the light quark masses and with f_q^N and δ_q^N, many authors provide constraints on the coefficients $C^S_{\alpha\beta}$ and $C^T_{\alpha\beta}$ rather than on the Lagragian parameters $\varepsilon^{qS}_{\alpha\beta}$ and $\varepsilon^{qT}_{\alpha\beta}$. In this paper, we choose instead to constrain the Lagragian parameters for fixed values of m_q, f_q^N and δ_q^N. It is straightforward to translate the current bounds and future sensitivity estimates on $\varepsilon^{qS}_{\alpha\beta}$ and $\varepsilon^{qT}_{\alpha\beta}$ presented in the next sections into constraints on $C^S_{\alpha\beta}$ and $C^T_{\alpha\beta}$.

Other authors, e.g. in Ref. [10, 12, 32, 51, 52], use the symbols C_S^q, C_V^q, C_T^q instead of ε^{qS}, ε^{qV}, ε^{qT} in Eqs. (7) to (9), with depending on the normalization convention either $C_V^q = \varepsilon^{qV}$ [52] (with the CEνNS cross section given by Eq. (6)) or $C_V^q = 2\varepsilon^{qV}$ [10, 12, 32, 51] (in which case one should replace $C^V_{\alpha\beta}$ by $\frac{1}{2}\, C^V_{\alpha\beta}$ in Eq. (6)).

III. EXPERIMENTAL SETUP AND DETECTORS

In this section, we describe the SNS neutrino beam and the main characteristics of the two detectors considered in this paper, namely the current CsI detector used by the COHERENT collaboration and a future NaI detector similar to the one under deployment by the same collaboration [53].

[2] In particular, we omit a scalar-tensor interference term in Eq. (6), which is proportional to T/E_ν and whose sign is different for neutrinos and antineutrinos [32].

A. Neutrino beam and predicted number of CEνNS events

At the SNS, the neutrinos used for CEνNS measurements arise from the decays at rest of the π^+ produced, together with neutrons and π^-'s, from the collision of high-energy protons on a mercury target (in which the π^- are absorbed before decaying). The SNS neutrino beam therefore consists of three components: a prompt, mono-energetic ν_μ component produced in the two-body decays of stopped positively charged pions ($\pi^+ \to \mu^+ + \nu_\mu$), and two delayed $\bar{\nu}_\mu$ and ν_e components arising from the subsequent decays at rest of the antimuons ($\mu^+ \to e^+ + \bar{\nu}_\mu + \nu_e$). These contributions can be analytically computed and are given by

$$\frac{dN_{\nu_\mu}}{dE_\nu} = \xi\,\delta\left(E_\nu - \frac{m_\pi^2 - m_\mu^2}{2m_\pi}\right), \tag{12}$$

$$\frac{dN_{\bar{\nu}_\mu}}{dE_\nu} = \xi\,\frac{64E_\nu^2}{m_\mu^3}\left(\frac{3}{4} - \frac{E_\nu}{m_\mu}\right), \tag{13}$$

$$\frac{dN_{\nu_e}}{dE_\nu} = \xi\,\frac{192E_\nu^2}{m_\mu^3}\left(\frac{1}{2} - \frac{E_\nu}{m_\mu}\right), \tag{14}$$

where E_ν is the neutrino energy and $\xi = rN_{\rm POT}/4\pi L^2$ is a normalization factor that depends on several experimental features: $N_{\rm POT}$, the number of protons on target (POT) throughout the operation time; r, the number of neutrinos per flavor produced by each POT; and L, the distance between the source and the detector.

Given the neutrino flux, the predicted number of CEνNS events in the nuclear recoil energy bin $[T_i, T_{i+1}]$ is given by, for a target material consisting of a single nucleus with mass M,

$$N_i^{th} = \mathcal{N}\int_{T_i}^{T_{i+1}} A(T)\,dT \int_0^{T'_{\rm max}} \mathcal{R}(T,T')\,dT' \sum_{\nu=\nu_e,\nu_\mu,\bar{\nu}_\mu} \int_{E_{\rm min}(T')}^{E_{\rm max}} dE_\nu\ \frac{{\rm d}N_\nu}{{\rm d}E_\nu}(E_\nu)\,\frac{{\rm d}\sigma}{{\rm d}T'}(E_\nu,T')\ , \tag{15}$$

where ${\rm d}\sigma/{\rm d}T$ is the relevant CEνNS cross section, given by Eq. (1) or (6), and $\mathcal{N} = N_A M_{\rm det}/M_{\rm mol}$ is the number of nuclei in the detector, which is computed from the detector mass $M_{\rm det}$ and the molar mass of the nucleus $M_{\rm mol}$, with N_A the Avogadro constant. The lower limit of the integral over E_ν is the minimal neutrino energy that can induce a nuclear recoil of energy T', $E_{\rm min}(T') = \sqrt{MT'/2}$, while the upper limit $E_{\rm max}$ is the maximum neutrino energy, which for the SNS beam is 52.8 MeV. Notice that Eq. (15) depends on both the real (T') and the reconstructed (T) nuclear recoil energies, with $\mathcal{R}(T,T')$ the smearing function, which may be different for each detector, and the upper limit of the integral over T' is the maximal nuclear recoil energy that can be induced by a neutrino from the beam, $T'_{\rm max} = 2E_{\rm max}^2/M$. Finally, $A(T)$ is an acceptance function, which also depends

Target nucleus	Z	N	Z/N	M (a.m.u)
Cs	55	78	0.71	132.91
I	53	74	0.72	126.90
Na	11	12	0.92	22.99

TABLE I. Main properties of the target nuclei used in the two detectors considered in this work: number of protons (Z) and neutrons (N), proton to neutron ratio (Z/N) and mass in atomic units (M).

on the detector. If the target material consists of two nuclei, as is the case for the CsI and NaI detectors, the total number of CEνNS events is the sum of the numbers of neutrino scatterings on each nucleus, computed separately from Eq. (15) with the appropriate values of M and $M_{\rm mol}$.

When the timing information of the experiment is available, one can also bin the data in time intervals. In this case, the predicted number of events in the nuclear recoil energy bin i and time bin j is given by

$$N_{ij}^{th} = \sum_{\nu=\nu_e,\nu_\mu,\overline{\nu}_\mu} N_{\nu,i}^{th} \int_{t_j}^{t_{j+1}} f_\nu(t)\, \varepsilon_t(t)\, dt\,, \tag{16}$$

where $N_{\nu,i}^{th}$ is the predicted number of CEνNS events induced by the component ν ($\nu = \nu_e, \nu_\mu, \overline{\nu}_\mu$) of the neutrino flux in the nuclear recoil energy bin $[T_i, T_{i+1}]$, $f_\nu(t)$ is the time distribution of the neutrino flux component ν taken from Ref. [54], and $\varepsilon(t)$ is the timing efficiency provided in Ref. [3]. To compute $N_{\nu,i}^{th}$, we use Eq. (15) without performing the sum over the contributions of the three components of the neutrino flux.

In our analysis, we will use the data of the current CsI detector of the COHERENT collaboration, as well as the expected future data from a NaI detector at the SNS. The main characteristics of these detectors are described in the following subsections.

B. Current CsI detector

The COHERENT collaboration performed CEνNS measurements with a 14.6 kg CsI detector located at 19.3 m from the neutrino source [3]. The accumulated data corresponds to $N_{POT} = 3.198 \times 10^{23}$, with a number of neutrinos per flavor of $r = 0.0848$ [3]. These numbers are used to compute the neutrino fluxes though Eqs. (12), (13) and (14). Following the COHERENT collaboration, we take the smearing function $\mathcal{R}(T, T')$ in Eq. (15) to be the Gamma function given in Ref. [3] (we refer the reader to Ref. [10] for details about the smearing procedure). Finally, we take into account the timing information provided by the COHERENT collaboration in our analysis and use Eq. (16) to compute the predicted number of events in each recoil energy and time bin.

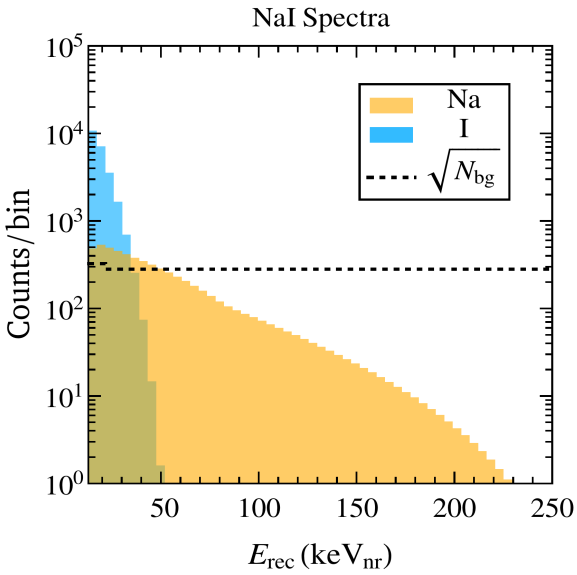

FIG. 1. Projected numbers of signal and background events in the SM as a function of the reconstructed nuclear recoil energy for the future NaI detector considered in this paper, assuming 3 years of data taking. The signal event spectra are displayed separately for the Sodium (yellow) and Iodine (light blue) target nuclei and include the contributions of the three components of the SNS neutrino beam (ν_e, ν_μ and $\overline{\nu}_\mu$). The expected steady-state background is represented by the black dashed curve, which for the sake of presentation shows the square root of the actual number of events.

C. Future NaI detector

The complete program of the COHERENT collaboration includes a NaI-based detector comprising several modules, each consisting of individual 7.7 kg NaI crystals [23]. In its final design, this detector is expected to have up to seven modules, each containing 63 crystals, giving a total mass $M_{\rm det} = 3395.7\,{\rm kg}$, which we shall consider in this work. The detector is expected to be located at a distance $L = 22\,{\rm m}$ from the neutrino source [23]. The SNS provides around $1.1{\times}10^{23}$ POT per calendar year, corresponding to $\simeq 5000$ hours (208.3 days) of operation per year. In this work, we consider three years of data taking with the SNS operating at current beam power, giving a total number of protons on target $N_{\rm POT} = 3.3 \times 10^{23}$. We also assume the current value of neutrinos per flavor, $r = 0.0848$. To compute the expected number of events, we assume a conservative constant acceptance of 80% and a Gaussian smearing function $\mathcal{R}(T, T')$ with an energy-dependent resolution $\sigma(T) = \eta\sqrt{TT_{th}}$, where[3] $\eta = 0.14$ and $T_{th} = 13\,{\rm keV_{nr}}$ is the nuclear recoil energy threshold of the detector [53].

[3] This choice reproduces the energy resolution given in [55] to a good approximation.

Under these assumptions and using the properties of the Sodium and Iodine nuclei given in Table I, we obtain the event spectra shown in Fig. 1, where the width of the recoil energy bins corresponds to 1 $\mathrm{keV_{ee}}$ [53]. To convert an electron recoil energy of 1 keV into the equivalent nuclear recoil energy (i.e., the nuclear recoil energy giving the same number of photoelectrons as an electron recoil energy of 1 keV), we use a constant quenching factor of 0.23 (estimated from Fig. 4.12 of Ref. [53]), resulting in a bin width of 4.33 $\mathrm{keV_{nr}}$. Fig. 1 displays the individual contributions of the Sodium (yellow) and Iodine (light blue) target nuclei to the signal event spectra. As can be seen, the CEνNS signal is dominated by the Iodine contribution below $T \approx 35\,\mathrm{keV_{nr}}$, while for larger nuclear recoil energies the Sodium contribution is dominant. This is due to the fact that the Iodine nucleus is heavier than Sodium, resulting in a larger cross section at low recoil energies, but in a lower endpoint (namely, $T_{\mathrm{max}}(\mathrm{I}) \approx 47\,\mathrm{keV_{nr}}$ while $T_{\mathrm{max}}(\mathrm{Na}) \approx 259\,\mathrm{keV_{nr}}$). As we will see later, the different features of the Sodium and Iodine contributions to the CEνNS signal can help reduce the degeneracies arising in the presence of vector-type GNIs. Fig. 1 also shows the expected steady-state background, which we assumed to be flat and equal to its average value of 300 ckkd (counts per keV_{ee} per kg per day) [53], except in the first two bins where the background is larger. There, we took a conservative value of 400 ckkd. In practice, the number of background events is reduced by a factor of 8000 [53] taking into account the fact that the SNS neutrino beam is pulsed. This reduction factor has been applied in Fig. 1. It is important to mention that the background model adopted here results in a smaller signal-over-background ratio than for the current CsI detector. For comparison, the signal-over-background ratio ranges from 4.2 $\times 10^{-3}$ to 0.15 in the first eight recoil energy bins of Fig. 1 (the ones that contribute the most to the statistics), while it varies between 0.04 and 2.2, depending on the energy bin, for the CsI measurement. This relatively large background level will affect the expected sensitivity of the NaI detector to generalized neutrino interactions. We will see in particular that, in spite of a larger statistics, the NaI detector will not be able to significantly improve the current CsI constraints on scalar and tensor GNI parameters.

IV. ANALYSIS PROCEDURE

For the analysis of the current CsI detector data, we follow the same procedure as Ref. [10] and use the Poissonian χ^2 function

$$\chi^2(\kappa) \,=\, \min_{\xi} \left\{ 2 \sum_{i,j} \left[N_{ij}(\kappa,\xi) - \tilde{N}_{ij} + \tilde{N}_{ij} \ln \left(\frac{\tilde{N}_{ij}}{N_{ij}(\kappa,\xi)} \right) \right] + \sum_{m=1}^{2} \frac{\xi_{sig,m}^2}{\sigma_{\xi_{sig,m}}^2} + \sum_{k=1}^{3} \frac{\xi_{bg,k}^2}{\sigma_{\xi_{bg,k}}^2} \right\}, \quad (17)$$

where i, j run over the nuclear recoil energy and time bins, respectively, $\tilde{N}_{ij}$ is the experimental number of events in bins (i, j), $N_{ij}(\kappa, \xi)$ the predicted number of events in the same bins in the presence of GNIs, κ stands for the set of GNI parameters under test, and ξ is the set of nuisance parameters over which we minimize the expression within braces. $N_{ij}(\kappa, \xi)$ is computed as

$$\begin{aligned} N_{ij}(\kappa,\xi) = \quad & (1+\xi_{sig,1})N_{ij}^{sig}(\kappa,\xi_{sig,2},\xi_1,\xi_2) + (1+\xi_{bg,1})N_{ij}^{BRN}(\xi_1) \\ & + (1+\xi_{bg,2})N_{ij}^{NIN}(\xi_1) + (1+\xi_{bg,3})N_{ij}^{SSB}, \end{aligned} \tag{18}$$

where N_{ij}^{sig} is the number of signal events, and N_{ij}^{BRN}, N_{ij}^{NIN} and N_{ij}^{SSB} are the numbers of beam-related neutron (BRN), neutrino-induced neutron (NIN) and steady-state (SSB) background events, respectively. The signal nuisance parameter $\xi_{sig,1}$ accounts for the detector efficiency, neutrino flux, and quenching factor (QF) normalizations, while $\xi_{sig,2}$ is related to the nuclear radius. The corresponding uncertainties are $\sigma_{\xi_{sig,1}} = 11.45\%$ and $\sigma_{\xi_{sig,2}} = 5\%$ [10]. As for the nuisance parameters $\xi_{bg,k}$, they are associated with the different sources of background: BRN ($\xi_{bg,1}$), NIN ($\xi_{bg,2}$) and SSB ($\xi_{bg,3}$), with corresponding uncertainties $\sigma_{\xi_{bg,1}} = 25\%$, $\sigma_{\xi_{bg,2}} = 35\%$ and $\sigma_{\xi_{bg,3}} = 2.1\%$ [3]. Following Ref. [10], we include in Eq. (17) two additional nuisance parameters ξ_1 and ξ_2, with no penalization term, which account for deviations in the uncertainty on the CEνNS detection efficiency and on beam timing, respectively. By minimizing over all nuisance parameters, we obtain allowed regions at a given confidence level for the GNI parameters under test.

To assess the sensitivity of the future NaI detector to GNI parameters, we consider the following χ^2 function

$$\chi^2(\kappa) = \min_{\xi} \left[\sum_i 2 \left\{ N_i(\kappa,\xi) - \tilde{N}_i + \tilde{N}_i \ln\left(\frac{\tilde{N}_i}{N_i(\kappa,\xi)}\right) \right\} + \left(\frac{\xi_{sig}}{\sigma_{sig}}\right)^2 + \left(\frac{\xi_{bg}}{\sigma_{bg}}\right)^2 \right], \tag{19}$$

where we have divided the data in recoil energy bins labelled by i. Since we are dealing with simulated data, we compare the theoretical predictions in the absence and in the presence of GNIs. Hence, we take

$$\tilde{N}_i = N_i^{sig}(SM) + N_i^{bg}\,, \tag{20}$$

where $N_i^{sig}(SM)$ represents the number of signal events in bin i predicted by the SM and N_i^{bg} is the simulated steady-state background described in Section III, while

$$N_i(\kappa,\xi) = N_i^{sig}(\kappa)(1+\xi_{sig}) + N_i^{bg}(1+\xi_{bg})\,, \tag{21}$$

where $N_i^{sig}(\kappa)$ is the predicted number of signal events in bin i in the presence of GNIs, and the nuisance parameters ξ_{sig}, ξ_{bg} account for the signal and background normalizations, respectively.

For the associated systematic uncertainties, we conservatively assume $\sigma_{sig} = 10\%$ and $\sigma_{bg} = 5\%$, motivated by the known values of the uncertainties for the current CsI detector. Notice that, due to the absence of detailed information on the signal and background systematic uncertainties, for the NaI detector currently under deployment at the SNS, we only consider two nuisance parameters.

V. EXPECTED SENSITIVITIES TO GNI PARAMETERS

In this section, we study the sensitivities to GNI parameters[4] of a future NaI detector with characteristics described in Subsection III C, and compare them with the constraints set by the COHERENT CsI detector. As discussed in Subsection II B, we consider only scalar, vector and tensor interactions and denote the corresponding couplings by $\varepsilon^{qS}_{\alpha\beta}$, $\varepsilon^{qV}_{\alpha\beta}$ and $\varepsilon^{qT}_{\alpha\beta}$, respectively, with $\alpha, \beta = e, \mu, \tau$ and $q = u, d$.

Since the SNS neutrino beam consists only of electron neutrinos, muon neutrinos and muon antineutrinos, not all of these parameters can be constrained by CEνNS measurements. Vector GNIs, also known as NSIs, are subject to the hermiticity condition $\varepsilon^{qV}_{\beta\alpha} = \left(\varepsilon^{qV}_{\alpha\beta}\right)^*$. As a result, there are 6 independent parameters for each quark flavor, but only 5 of them can be constrained at the SNS: two real flavor-diagonal couplings, ε^{qV}_{ee} and $\varepsilon^{qV}_{\mu\mu}$, and three complex flavor off-diagonal couplings, $\varepsilon^{qV}_{e\mu}$, $\varepsilon^{qV}_{e\tau}$ and $\varepsilon^{qV}_{\mu\tau}$. In this paper, we study the sensitivities of the CsI and NaI detectors to ε^{qV}_{ee}, $\varepsilon^{qV}_{\mu\mu}$ and $\varepsilon^{qV}_{e\mu}$ $(q = u, d)$, leaving aside the other off-diagonal couplings, which are less constrained[5].

For scalar and tensor GNIs, the number of independent parameters depends on whether neutrinos are Dirac of Majorana fermions. In this paper, we assume that they are Majorana fermions, both for simplicity and because this possibility is better motivated from a theoretical point of view. Scalar couplings are therefore symmetric, and for each quark flavor, 5 out of the 6 independent ones can be constrained by CEνNS measurements at the SNS. However, due to the absence of interference between the scalar and SM contributions to the CEνNS cross section, the same constraints apply to ε^{qS}_{ee} and $\varepsilon^{qS}_{e\tau}$, as well as to $\varepsilon^{qS}_{\mu\mu}$ and $\varepsilon^{qS}_{\mu\tau}$. It is therefore sufficient to study the sensitivities of the CsI and NaI detectors to the scalar couplings ε^{qS}_{ee}, $\varepsilon^{qS}_{\mu\mu}$ and $\varepsilon^{qS}_{e\mu}$ $(q = u, d)$. Finally, tensor couplings are antisymmetric for Majorana neutrinos, leaving only 3 indepedent parameters $\varepsilon^{qT}_{e\mu}$, $\varepsilon^{qT}_{e\tau}$ and $\varepsilon^{qT}_{\mu\tau}$ for each value of q, all of which can induce scatterings of SNS neutrinos off nuclei.

Throughout this paper, we assume all GNI couplings to be real. The upper bounds on these

[4] From now on, we will collectively refer to vector, scalar and tensor couplings as GNI parameters, and we will more specifically use NSI parameters for vector couplings.

[5] This is due to the fact that $\varepsilon^{qV}_{e\mu}$ can induce coherent scatterings for all three components of the SNS neutrino flux, while only ν_e (resp. ν_μ and $\nu_{\bar{\mu}}$) can scatter off a nucleus via $\varepsilon^{qV}_{e\tau}$ (resp. $\varepsilon^{qV}_{\mu\tau}$).

parameters obtained from the currently available CsI data and the expected sensitivity of the future NaI detector are determined following the numerical procedure described in Section IV.

A. Expected sensitivities to individual GNI parameters

We first consider the expected sensitivities of the NaI detector to individual GNI parameters, i.e. we consider a single nonvanishing coupling at a time. Note that in this case, the assumption of real couplings does not mean any loss of generality, as the CEνNS cross section only depends on the moduli of the GNI parameters (except for diagonal vector couplings, which are real and can interfere with the SM contribution).

The results for vector couplings are shown in Fig. 2, where the $\Delta\chi^2$ functions defined in Section IV are plotted against the parameter assumed to be nonvanishing (from left to right: ε_{ee}^{qV}, $\varepsilon_{e\mu}^{qV}$ and $\varepsilon_{\mu\mu}^{qV}$, with $q = u$ in the upper panels and $q = d$ in the lower panels). The black solid curves are obtained using the currently available CsI data, and are consistent with the results obtained in Ref. [10]. The red dashed curves represent the expected sensitivities of the future NaI detector after 3 years of data taking, assuming conservatively $\sigma_{sig} = 10\%$ and $\sigma_{bg} = 5\%$. For the flavor-diagonal parameters ε_{ee}^{qV} and $\varepsilon_{\mu\mu}^{qV}$ $(q = u, d)$, two minima can be observed in the $\Delta\chi^2$ profiles[6], as a result of the interference between the SM and NSI contributions in the CEνNS cross section, Eq. (6). The sharp rise of the $\Delta\chi^2$ for $\varepsilon_{\mu\mu}^{qV}$ between the two minima is due to the fact that when $\varepsilon_{\mu\mu}^{qV} \approx 0.2$, the NSI and SM contributions to the CEνNS cross section almost completely cancel out for ν_μ's and $\bar{\nu}_\mu$'s, resulting in a reduction of the predicted number of CEνNS events by roughly 2/3, in strong tension with data. The same effect is present for ε_{ee}^{qV}, but since this coupling only affects ν_e-induced CEνNS events, i.e. roughly 1/3 of the signal, the $\Delta\chi^2$ reaches smaller values between the two minima (especially for CsI, which suffers from a smaller statistics than the NaI detector). In Table II, we give the 90% C.L. and 2σ expected sensitivities of the future NaI detector to the vector couplings ε_{ee}^{qV}, $\varepsilon_{e\mu}^{qV}$ and $\varepsilon_{\mu\mu}^{qV}$ $(q = u, d)$, as well as the constraints on these parameters from the COHERENT CsI data.

As can be seen from Fig. 2 and Table II, a clear improvement of the constraints on these diagonal vector couplings is expected from the future NaI detector, already with 3 years of data taking. This is partly due to the larger statistics of the NaI detector, as already mentioned. However, the most noticeable feature, namely the fact that the second minimum of the χ^2 function tends to

[6] Note that for the CsI detector, the first minimum of the χ^2 function is not located at $\varepsilon_{ee}^{qV} = 0$ (resp. $\varepsilon_{\mu\mu}^{qV} = 0$). This is due to the fact that we are analysing real data, which does not exactly match the SM prediction.

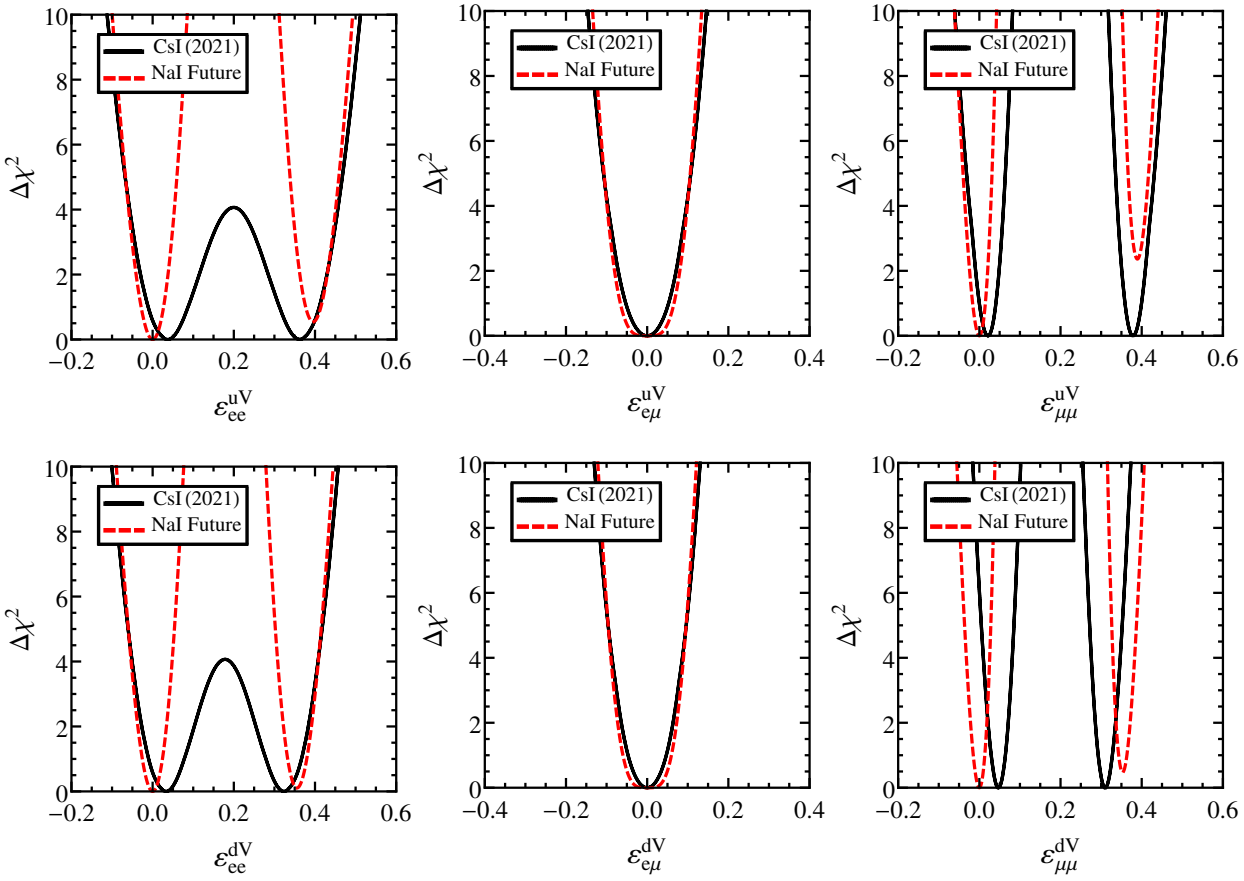

FIG. 2. One-dimensional $\Delta\chi^2$ profiles (17) and (19) for the vector coupling ε_{ee}^{qV} (left panels), $\varepsilon_{e\mu}^{qV}$ (middle panels) and $\varepsilon_{\mu\mu}^{qV}$ (right panels), with $q = u$ in the upper panels and $q = d$ in the lower panels. The black solid curves correspond to Eq. (17) and are obtained using the currently available data of the COHERENT CsI detector. The red dashed curves correspond to Eq. (19) and represent the expected sensitivities of the NaI detector described in Subsection III C, assuming 3 years of data taking at the SNS. The off-diagonal NSI parameter $\varepsilon_{e\mu}^{qV}$ is assumed to be real.

be disfavoured (mostly for the parameter $\varepsilon_{\mu\mu}^{uV}$, and to a lesser extent for ε_{ee}^{uV} and $\varepsilon_{\mu\mu}^{dV}$), cannot be explained by statistics alone. This can be understood instead by noting that the SM–NSI interference term in the CEνNs cross section is controlled by the quantity (where we have neglected a term suppressed by $g_V^p \ll 1$)

$$C_{\alpha\alpha}^V + Q_{W,\alpha} \simeq N \left[\left(2\,\frac{Z}{N} + 1 \right) \varepsilon_{\alpha\alpha}^{uV} + \left(\frac{Z}{N} + 2 \right) \varepsilon_{\alpha\alpha}^{dV} - \frac{1}{2} \right], \tag{22}$$

and is therefore sensitive to the proton to neutron ratio of the target nucleus. In particular, the second $\Delta\chi^2$ minimum for $\varepsilon_{\alpha\alpha}^{uV}$ (resp. $\varepsilon_{\alpha\alpha}^{dV}$) is located at $\varepsilon_{\alpha\alpha}^{uV} \approx 1/(2Z/N + 1)$ (resp. $\varepsilon_{\alpha\alpha}^{dV} \approx 1/(Z/N + 2)$). While the CsI detector involves two nuclei with approximately the same proton

Detector	q	ε_{ee}^{qV}		$\varepsilon_{e\mu}^{qV}$		$\varepsilon_{\mu\mu}^{qV}$	
		90% C.L.	2σ C.L.	90% C.L.	2σ C.L.	90% C.L.	2σ C.L.
NaI	u	$[-0.047, 0.044]$ $\cup [0.356, 0.438]$	$[-0.059, 0.053]$ $\cup [0.345, 0.451]$	$[-0.088, 0.088]$	$[-0.099, 0.099]$	$[-0.027, 0.024]$ $\cup [0.380, 0.399]$	$[-0.036, 0.028]$ $\cup [0.371, 0.411]$
	d	$[-0.043, 0.039]$ $\cup [0.317, 0.398]$	$[-0.053, 0.048]$ $\cup [0.308, 0.408]$	$[-0.079, 0.079]$	$[-0.09, 0.09]$	$[-0.026, 0.021]$ $\cup [0.333, 0.376]$	$[-0.032, 0.026]$ $\cup [0.329, 0.382]$
CsI	u	$[-0.04, 0.134]$ $\cup [0.266, 0.440]$	$[-0.056, 0.186]$ $\cup [0.212, 0.456]$	$[-0.081, 0.081]$	$[-0.097, 0.097]$	$[-0.015, 0.053]$ $\cup [0.346, 0.414]$	$[-0.024, 0.060]$ $\cup [0.34, 0.424]$
	d	$[-0.035, 0.120]$ $\cup [0.237, 0.393]$	$[-0.05, 0.168]$ $\cup [0.190, 0.408]$	$[-0.073, 0.073]$	$[-0.087, 0.087]$	$[-0.016, 0.075]$ $\cup [0.282, 0.340]$	$[-0.010, 0.081]$ $\cup [0.276, 0.347]$

TABLE II. Sensitivities to the vector couplings ε_{ee}^{qV}, $\varepsilon_{e\mu}^{qV}$ and $\varepsilon_{\mu\mu}^{qV}$ ($q = u, d$) at the 90% and 2σ confidence levels with 1 degree of freedom (i.e. $\Delta\chi^2 \leq 2.71$ and $\Delta\chi^2 \leq 4$, respectively). For the CsI detector, the intervals actually correspond to the ranges of parameter values allowed by the currently available data, while for the NaI detector they represent the expected sensitivities assuming 3 years of data taking at the SNS. The off-diagonal NSI parameter $\varepsilon_{e\mu}^{qV}$ is assumed to be real.

to neutron ratio, this is not the case for the NaI detector (see Table I), making it more difficult to fit SM-like experimental data with a nonzero value of $\varepsilon_{\alpha\alpha}^{uV}$ or $\varepsilon_{\alpha\alpha}^{dV}$. The same effect is observed when combining the data collected by two detectors with target nuclei characterized by different proton to neutron ratios [24, 39]; in the case of the NaI detector, the two nuclei are present in the same target. However, the NaI detector considered in this paper is not as efficient at constraining flavor-diagonal vector couplings as expected from suitably chosen combinations of the detectors proposed for CEνNS measurements at the European Spallation Source [24], such as CsI + Si and Xe + Si [39]. The latter indeed benefit from a large statistics and from a lower background level than the NaI detector. Also, the advantage of combining two target nuclei with different proton to neutron ratios in the same detector is counterbalanced, in the case of NaI, by the fact that the recoil energy bins in which the Na-induced scatterings contribute significantly are the ones in which the signal over background ratio is the least favorable, as can be seen from Fig. 1.

For off-diagonal vector couplings, whose contributions do not interfere with the SM one, no significant improvement on the current constraints is expected from the future NaI detector, in spite of the larger statistics (the results for $\varepsilon_{e\tau}^{qV}$ and $\varepsilon_{\mu\tau}^{qV}$ are qualitatively similar to the ones for $\varepsilon_{e\mu}^{qV}$ shown in Fig. 2). This is due to the fact that the signal-over-background ratio is significantly smaller than for the CsI detector (see the discussion at the end of Subsection III C).

Let us now move on to the results for scalar GNIs. As explained before, CEνNS measurements

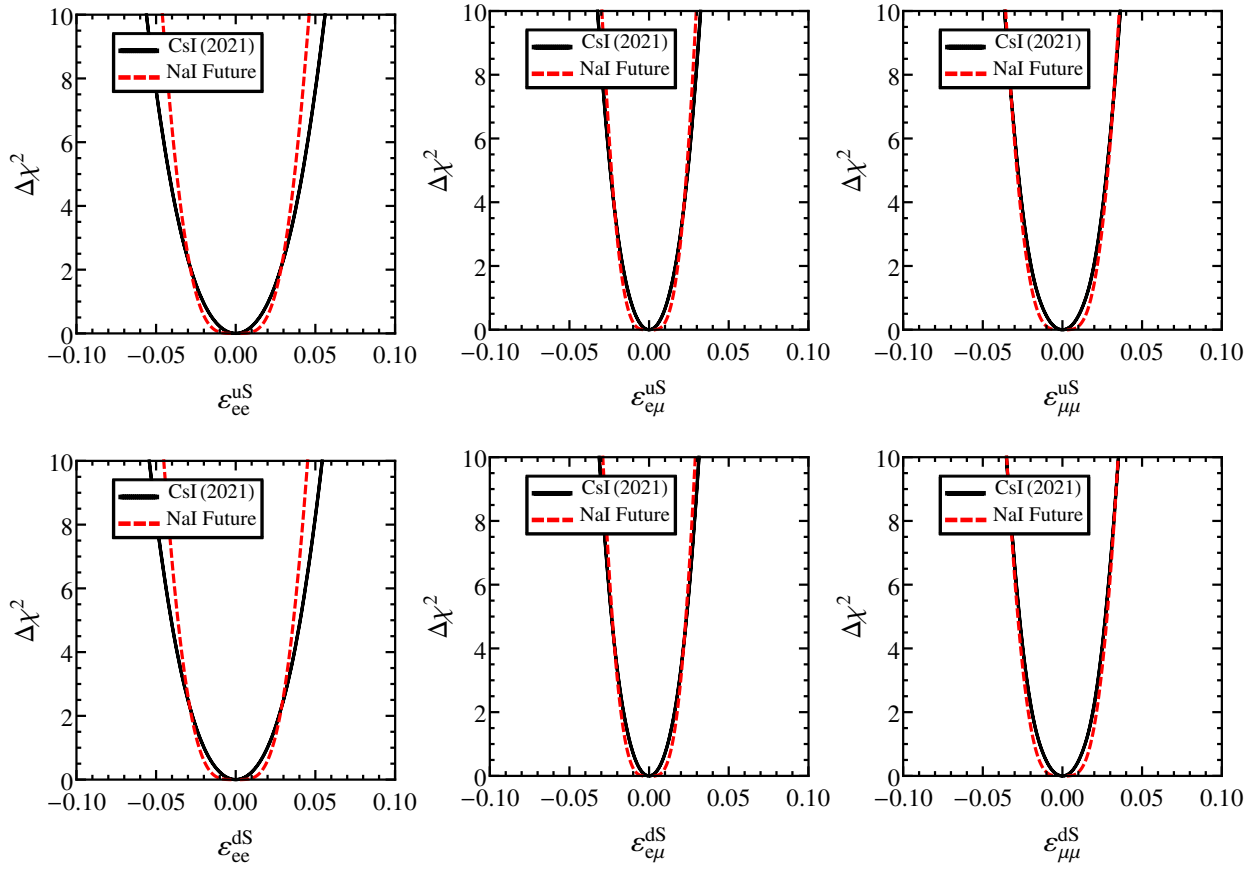

FIG. 3. Same as Fig. 2, but for the scalar couplings ε^{qS}_{ee} (left panels), $\varepsilon^{qS}_{e\mu}$ (middle panels) and $\varepsilon^{qS}_{\mu\mu}$ (right panels), with $q = u$ in the upper panels and $q = d$ in the lower panels. All couplings are assumed to be real.

Detector	q	ε^{qS}_{ee}		$\varepsilon^{qS}_{e\mu}$		$\varepsilon^{qS}_{\mu\mu}$	
		90% C.L.	2σ C.L.	90% C.L.	2σ C.L.	90% C.L.	2σ C.L.
NaI	u	$[-0.031, 0.031]$	$[-0.034, 0.034]$	$[-0.02, 0.02]$	$[-0.022, 0.022]$	$[-0.024, 0.024]$	$[-0.027, 0.027]$
	d	$[-0.031, 0.031]$	$[-0.033, 0.033]$	$[-0.019, 0.019]$	$[-0.021, 0.021]$	$[-0.023, 0.023]$	$[-0.026, 0.026]$
CsI	u	$[-0.032, 0.032]$	$[-0.038, 0.038]$	$[-0.018, 0.018]$	$[-0.022, 0.022]$	$[-0.022, 0.022]$	$[-0.026, 0.026]$
	d	$[-0.031, 0.031]$	$[-0.037, 0.037]$	$[-0.018, 0.018]$	$[-0.022, 0.022]$	$[-0.022, 0.022]$	$[-0.025, 0.025]$

TABLE III. Same as Table II, but for the scalar couplings ε^{qS}_{ee}, $\varepsilon^{qS}_{e\mu}$ and $\varepsilon^{qS}_{\mu\mu}$ ($q = u$, d).

at the SNS only give six independent contraints on scalar couplings, since $\varepsilon^{qS}_{e\tau}$ and $\varepsilon^{qS}_{\mu\tau}$ contribute the same way to the CEνNS cross section as ε^{qS}_{ee} and $\varepsilon^{qS}_{\mu\mu}$, respectively[7]. We therefore only present results for the 6 scalar couplings ε^{qS}_{ee}, $\varepsilon^{qS}_{\mu\mu}$ and $\varepsilon^{qS}_{e\mu}$ ($q = u, d$). The $\Delta\chi^2$ profiles are displayed in Fig. 3, and the 90% C.L. and 2σ expected sensitivities of the future NaI detector, together

[7] This statement holds for symmetric scalar couplings, hence for Majorana neutrinos (as assumed in this paper), but not for Dirac neutrinos.

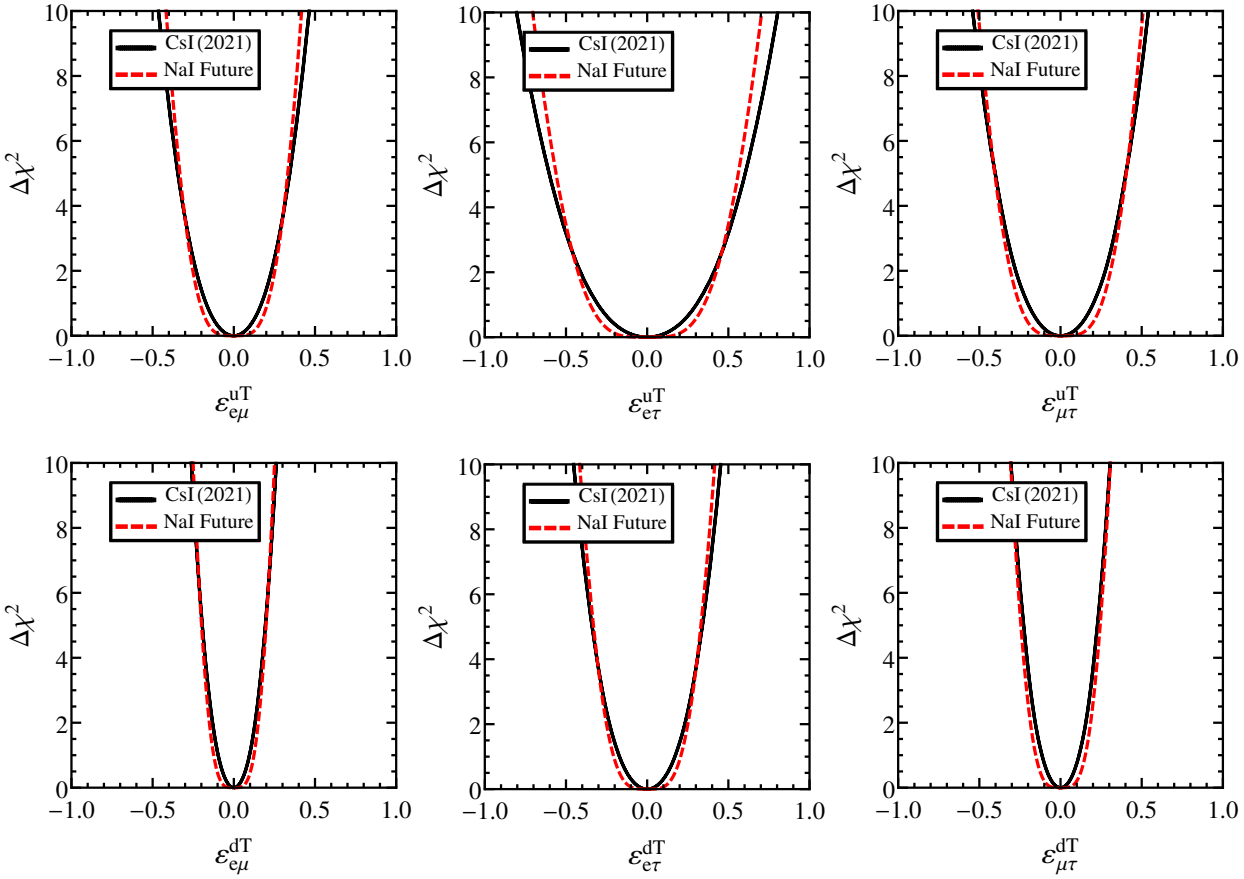

FIG. 4. Same as Fig. 2, but for the tensor couplings $\varepsilon^{qT}_{e\mu}$ (left panels), $\varepsilon^{qT}_{e\tau}$ (middle panels) and $\varepsilon^{qT}_{\mu\tau}$ (right panels), with $q = u$ in the upper panels and $q = d$ in the lower panels. All couplings are assumed to be real.

with the constraints from the COHERENT CsI data, are given in Table III. As can be seen by comparing Figs. 2 and 3, the results for scalar couplings are similar to the ones for off-diagonal vector couplings, which is not a surprise since both types of interactions share the property of not interfering with the SM contribution in the CEνNS cross section. In particular, we do not expect the future NaI detector to significantly improve the current CsI constraints on scalar couplings within the assumptions made in our analysis (3 years of running time, $\sigma_{sig} = 10\%$ and $\sigma_{bg} = 5\%$). Note however that, at the $\gtrsim 3\sigma$ confidence level, there is a slight improvement for ε^{uS}_{ee} and ε^{dS}_{ee}.

Finally, the results for tensor GNIs are shown in Fig. 4 and Table IV. Recall that there are only 6 independent tensor couplings if, as assumed in this paper, neutrinos are Majorana fermions, namely $\varepsilon^{qT}_{e\mu}$, $\varepsilon^{qT}_{e\tau}$ and $\varepsilon^{qT}_{\mu\tau}$ $(q = u, d)$. Comparing the expected sensitivities of the future NaI detector with the constraints from the COHERENT CsI data (see Table IV), we only expect a marginal improvement of the constraints on tensor GNI paremeters. However, at the $\gtrsim 3\sigma$ confidence level,

Detector	q	$\varepsilon^{qT}_{e\mu}$		$\varepsilon^{qT}_{e\tau}$		$\varepsilon^{qT}_{\mu\tau}$	
		90% C.L.	2σ C.L.	90% C.L.	2σ C.L.	90% C.L.	2σ C.L.
NaI	u	$[-0.275, 0.275]$	$[-0.310, 0.310]$	$[-0.465, 0.465]$	$[-0.525, 0.525]$	$[-0.337, 0.337]$	$[-0.380, 0.380]$
	d	$[-0.165, 0.165]$	$[-0.186, 0.186]$	$[-0.274, 0.274]$	$[-0.310, 0.310]$	$[-0.203, 0.203]$	$[-0.228, 0.228]$
CsI	u	$[-0.265, 0.265]$	$[-0.314, 0.314]$	$[-0.467, 0.467]$	$[-0.55, 0.55]$	$[-0.314, 0.314]$	$[-0.369, 0.369]$
	d	$[-0.15, 0.15]$	$[-0.177, 0.177]$	$[-0.264, 0.264]$	$[-0.310, 0.310]$	$[-0.177, 0.177]$	$[-0.208, 0.208]$

TABLE IV. Same as Table II, but for the tensor couplings $\varepsilon^{qT}_{e\mu}$, $\varepsilon^{qT}_{e\tau}$ and $\varepsilon^{qT}_{\mu\tau}$ ($q = u, d$).

a slight improvement can be observed for $\varepsilon^{uT}_{e\tau}$.

B. Expected sensitivities to pairs of GNI parameters

In this section, we study the expected sensitivity of the NaI detector to pairs of GNI parameters, i.e. we consider two nonvanishing couplings at a time. As it is well known, this situation leads to degeneracies in the form of extended allowed regions in the two-dimensional GNI parameter space. Combining data on target nuclei characterized by different proton to neutron ratios can help reduce these degeneracies, as shown e.g. in Refs. [8, 24, 39]. In the case of the NaI detector studied in this paper, the two nuclei have significantly different proton to neutron ratios 0.92 (for Na) and 0.72 (for I), while the Cesium and Iodine targets of the CsI detector have approximately the same ratio.

We begin our analysis by considering the case where the two nonvanishing GNI parameters are of vector type (i.e., NSIs). Many different combinations of two NSI parameters are possible; we only present results for a few representative examples, as the other combinations are characterized by similar allowed regions. Fig. 5 shows the allowed regions at the 90% confidence level for four different pairs of vector couplings. The upper panels correspond to combinations of diagonal couplings involving the same lepton flavor but different quarks, namely $\left(\varepsilon^{uV}_{ee}, \varepsilon^{dV}_{ee}\right)$ in the left panel and $\left(\varepsilon^{uV}_{\mu\mu}, \varepsilon^{dV}_{\mu\mu}\right)$ in the right panel. By contrast, the lower panels correspond to pairs of vector couplings involving the same quark but different lepton flavors. The combination in the left panel, $\left(\varepsilon^{uV}_{ee}, \varepsilon^{uV}_{\mu\mu}\right)$, involves two diagonal couplings, while the one in the right panel, $\left(\varepsilon^{uV}_{e\mu}, \varepsilon^{uV}_{\mu\mu}\right)$, involves a diagonal and an off-diagonal coupling. In all cases, the green regions are the ones allowed by the current CsI data (these allowed regions were first presenteded in Ref. [10], and are shown here for reference), while the regions delimited by red lines correspond to the expected sensitivity of the NaI detector described in Subsection III C, assuming 3 years of data taking at the SNS.

In the upper panels of Fig. 5, the allowed regions consist of two parallel bands [9]. This is a

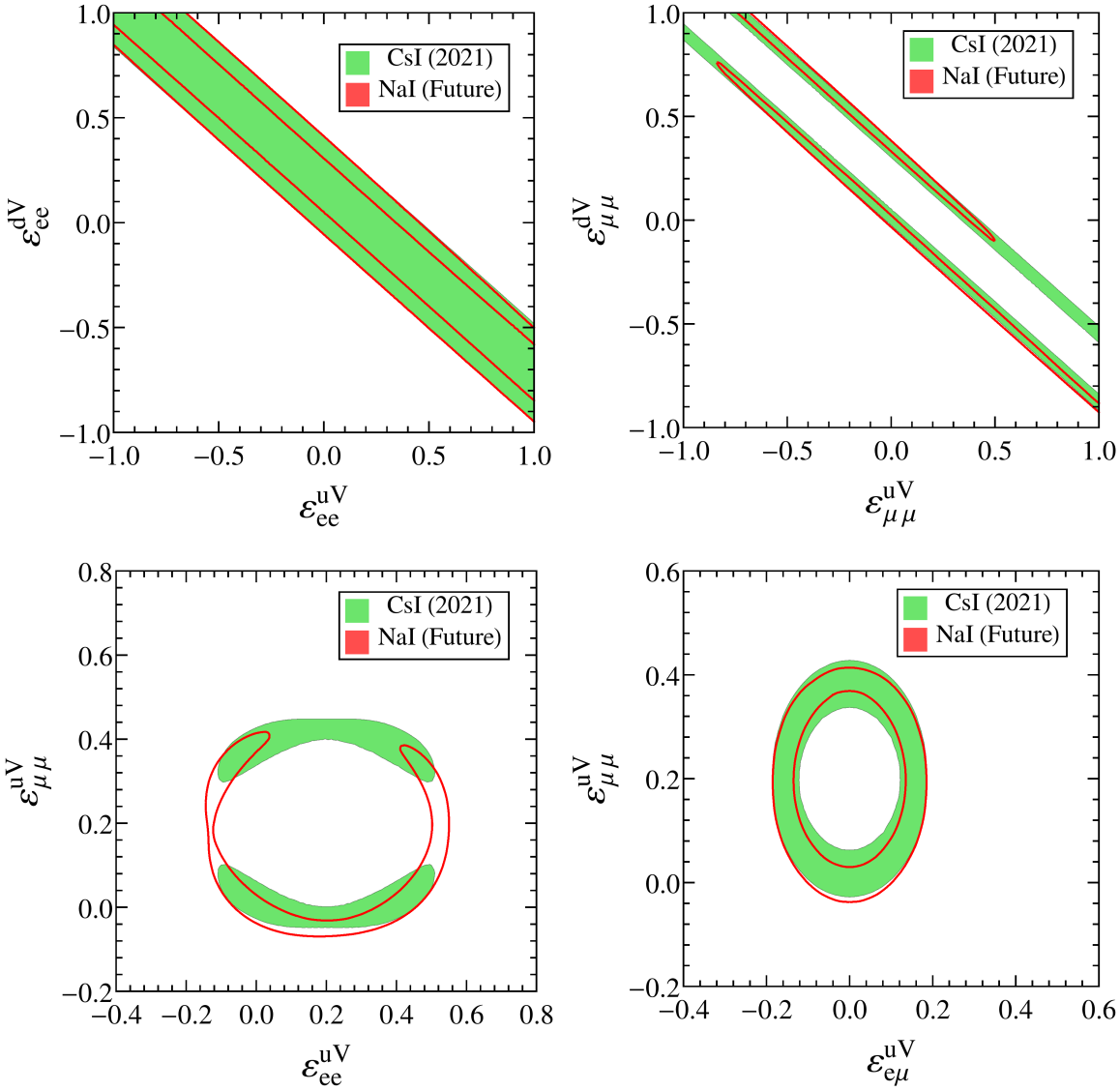

FIG. 5. 90% C.L. allowed regions (with two degrees of freedom, i.e. $\Delta\chi^2 \leq 4.61$) for different combinations of two NSI parameters: $(\varepsilon^{uV}_{ee}, \varepsilon^{dV}_{ee})$ (upper left panel), $(\varepsilon^{uV}_{\mu\mu}, \varepsilon^{dV}_{\mu\mu})$ (upper right panel), $(\varepsilon^{uV}_{ee}, \varepsilon^{uV}_{\mu\mu})$ (lower left panel) and $(\varepsilon^{uV}_{e\mu}, \varepsilon^{uV}_{\mu\mu})$ (lower right panel). The green regions correspond to the constraints from the current CsI data, while the red contours represent the expected sensitivity of the NaI detector described in Subsection III C, assuming 3 years of data taking at the SNS. The off-diagonal parameter $\varepsilon^{qV}_{e\mu}$ is assumed to be real.

consequence of the fact that, for a single-nucleus target (or a target composed of two nuclei with approximately the same proton to neutron ratio, like CsI), the CEνNS cross section depends on NSI parameters only through the modulus of the combination (22), which can be more conveniently

rewritten as

$$C_{\alpha\alpha}^{V} + Q_{W,\alpha} \simeq (Z+2N)\left(\varepsilon_{\alpha\alpha}^{dV} - m\,\varepsilon_{\alpha\alpha}^{uV}\right) - \frac{1}{2}\,, \qquad m = -\frac{2Z+N}{Z+2N}\,. \tag{23}$$

Thus, values of $\varepsilon_{\alpha\alpha}^{uV}$ and $\varepsilon_{\alpha\alpha}^{dV}$ lying on a straight ligne with slope m [8] produce the same number of CEνNS events in each recoil energy bin. This is an example of the degeneracies mentioned above. It follows that the parameter space region allowed by SM-like experimental data at a given confidence interval (here 90% C.L.) consists of two parallel bands around the straight lines $\varepsilon_{\alpha\alpha}^{dV} - m\,\varepsilon_{\alpha\alpha}^{uV} = 0$ and $\varepsilon_{\alpha\alpha}^{dV} - m\,\varepsilon_{\alpha\alpha}^{uV} = 1/(Z+2N)$. This is what can be observed in Fig. 5 for CsI, where the two bands overlap for $\alpha = e$ due to the limited statistics (there are twice as many ν_μ's and $\overline{\nu}_\mu$'s as ν_e's in the SNS neutrino beam). For NaI, the bands are thinner due to the larger statistics, and they reduce to closed or semi-closed areas in the $(\varepsilon_{\mu\mu}^{uV},\, \varepsilon_{\mu\mu}^{dV})$ plane[8]. This partial breaking of the degeneracy between $\varepsilon_{\mu\mu}^{uV}$ and $\varepsilon_{\mu\mu}^{dV}$ is due to the fact that Sodium and Iodine have different proton to neutron ratios, hence different slopes m_I and m_{Na}.

The elliptic-like shape of the allowed regions in the lower panels of Fig. 5 can be understood from the expression for the predicted CEνNS events in each reconstructed nuclear recoil energy bin [39]. Considering for instance the couplings $\left(\varepsilon_{ee}^{uV},\, \varepsilon_{\mu\mu}^{uV}\right)$, the predicted number of events in the recoil energy bin $[T_i, T_{i+1}]$, for a single-nucleus detector, can be written as

$$N_i^{th} = C_i^e\,(2Z+N)^2\left(\varepsilon_{ee}^{uV} + \frac{Zg_V^p + Ng_V^n}{2Z+N}\right)^2 + C_i^\mu\,(2Z+N)^2\left(\varepsilon_{\mu\mu}^{uV} + \frac{Zg_V^p + Ng_V^n}{2Z+N}\right)^2\,, \tag{24}$$

where C_i^e (resp. C_i^μ) is the number obtained by performing the integral over E_{ν_e} (resp. E_{ν_μ} and $E_{\overline{\nu}_\mu}$) and the true and reconstructed nuclear recoil energies in Eq. (15), after having factorized out $|C_{\alpha\alpha}^V + Q_{W,\alpha}|^2$. Eq. (24) is the equation of an ellipse with semi-major and semi-minor axes (given respectively by $\sqrt{N_i^{th}/C_i^e\,(2Z+N)^2}$ and $\sqrt{N_i^{th}/C_i^\mu\,(2Z+N)^2}$) that depend on both the nucleus and the energy bin (the center of the ellipse also depends on the nucleus). All sets of $(\varepsilon_{ee}^{uV},\, \varepsilon_{\mu\mu}^{uV})$ values lying on this ellipse predict the same number of CEνNS events in the ith energy bin, but not necessarily in the other bins, resulting in an approximate degeneracy between these two parameters. This explains why the 90% C.L. allowed regions in the lower left panel of Fig. 5 have the form of approximate, partly broken ellipses. The degeneracy is broken by the energy binning and, in the case of the NaI detector, by the fact that the nuclei composing the target have different numbers of protons and neutrons (while they are approximately the same for Cesium and Iodine).

From the lower left panel of Fig. 5, one can see that the CsI and NaI detectors play a complementary role in reducing the degeneracy between the vector couplings ε_{ee}^{uV} and $\varepsilon_{\mu\mu}^{uV}$. For CsI, the

[8] The same effect should occur for $(\varepsilon_{ee}^{uV},\, \varepsilon_{ee}^{dV})$ as well, but is not seen in the left panel of Fig. 5 due to the relatively smaller statistics of the ν_e beam component with respect to the $\nu_\mu + \overline{\nu}_\mu$ components.

allowed region has a symmetric shape, reflecting the fact that Cesium and Iodine have almost the same numbers of protons and neutrons. There are no allowed points around $\varepsilon_{\mu\mu}^{uV} \approx 0.2$, where the NSI and SM contributions to ν_μ- and $\overline{\nu}_\mu$-induced CEνNS almost completely cancel out. While an increase of the number of ν_e-induced CEνNS events could in principle compensate for this effect, the required increase (hence the required value of ε_{ee}^{uV}) is not the same in all energy bins, so that no value of ε_{ee}^{uV} can mimic the experimental data within 90% C.L. A similar effect occurs around $\varepsilon_{ee}^{uV} \approx 0.2$, but only leads to a small shriking of the allowed region. By contrast, the expected allowed region for NaI is not symmetric. Around $\varepsilon_{ee}^{uV} \approx 0.2$, negative values of $\varepsilon_{\mu\mu}^{uV}$ can compensate for the suppression of ν_e-induced CEνNS events, but this is not possible for positive values of $\varepsilon_{\mu\mu}^{uV}$, as a consequence of the different proton to neutron ratios of the Sodium and Iodine nuclei[9]. Around $\varepsilon_{\mu\mu}^{uV} \approx 0.2$, the allowed region shrinks for negative values of ε_{ee}^{uV}, but the degeneracy is not completely broken.

Finally, we also observe an "ellipse-shaped" degeneracy between the vector couplings $\varepsilon_{e\mu}^{uV}$ and $\varepsilon_{\mu\mu}^{uV}$ in the lower right panel of Fig. 5, but neither the CsI nor the NaI detector are able to reduce this degeneracy. This can be understood by noting that $\varepsilon_{e\mu}^{uV}$ induces both ν_e and $\nu_\mu/\overline{\nu}_\mu$ coherent scatterings on the target nuclei, without interfering with the SM contribution. Nonvanishing values of $\varepsilon_{e\mu}^{uV}$ can therefore compensate for the destructive interference between the SM and $\varepsilon_{\mu\mu}^{uV}$ contributions to the CEνNS cross section, which would otherwise reduce the number of $\nu_\mu/\overline{\nu}_\mu$-induced signal events. As a result, the ellipse is not broken around $\varepsilon_{\mu\mu}^{uV} \approx 0.2$ in the case of the CsI detector, at variance with what one can see in the lower left panel. The expected sensitivity of the future NaI detector only represents a slight improvement on the CsI constraints. In particular, we do not observe a partial breaking of the degeneracy around $\varepsilon_{\mu\mu}^{uV} \approx 0.4$, unlike in the lower left panel.

Let us now consider scalar and tensor GNIs. Fig. 6 shows the 90% C.L. allowed regions for two different pairs of scalar couplings with the same lepton flavor indices, $\left(\varepsilon_{e\mu}^{uS}, \varepsilon_{e\mu}^{dS}\right)$ in the left panel and $\left(\varepsilon_{\mu\mu}^{uS}, \varepsilon_{\mu\mu}^{dS}\right)$ in the right panel. As in Fig. 5, the regions allowed by the current CsI data are in green, while the ones delimited by red lines correspond to the expected sensitivity of the future NaI detector, assuming 3 years of data taking at the SNS. Since the scalar couplings $\varepsilon_{\alpha\beta}^{uS}$ and $\varepsilon_{\alpha\beta}^{dS}$ contribute to the CEνNS cross section through the linear combination $C_{\alpha\beta}^{S}$, given in Eq. (7), the allowed regions are straight bands around a line passing through the origin (as a consequence of the fact that scalar couplings do not interfere with the SM contribution). While the slope of this line depends on the proton to neutron ratio of the target nucleus, it is in practice very close to -1

[9] The same asymmetric behaviour can be seen in the $\Delta\chi^2$ for $\varepsilon_{\mu\mu}^{uV}$, in the upper right panel of Fig. 2, where the second minimum is "uplifted" with respect to the first one, a feature that is not observed in the case of the CsI detector.

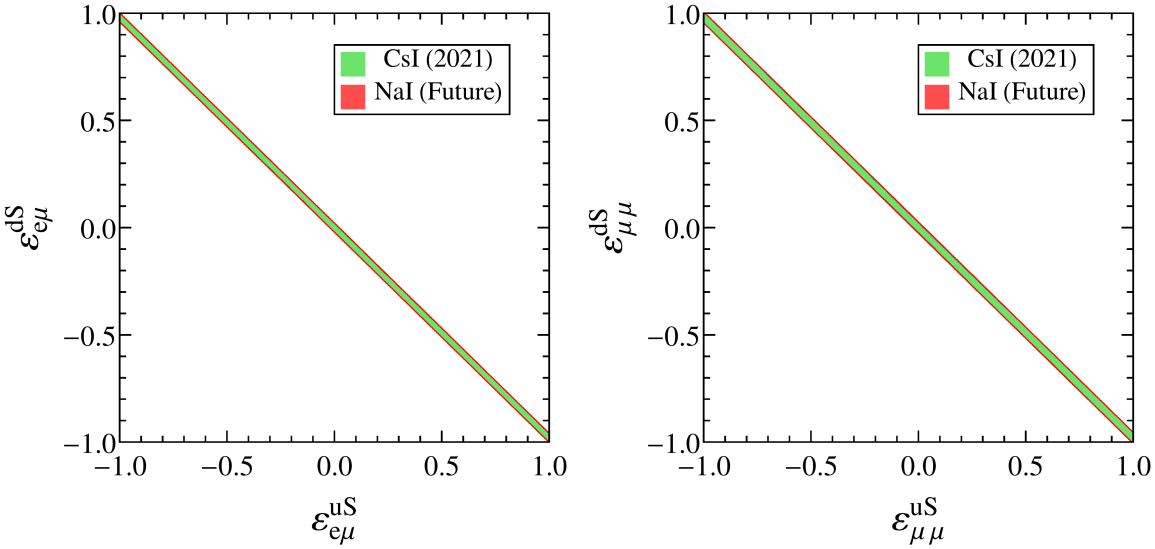

FIG. 6. 90% C.L. allowed regions for the pairs of scalar GNI parameters $\left(\varepsilon^{uS}_{e\mu}, \varepsilon^{dS}_{e\mu}\right)$ (left panel) and $\left(\varepsilon^{uS}_{\mu\mu}, \varepsilon^{dS}_{\mu\mu}\right)$ (right panel). The green regions correspond to the constraints from the current CsI data, while the red contours represent the expected sensitivity of the NaI detector described in Subsection III C, assuming 3 years of data taking at the SNS. All GNI parameters are assumed to be real.

for Cs, I and Na, as can be seen in Fig. 6. A consequence of this is that even though Sodium and Iodine have different proton to neutron ratios, the NaI detector is unable to reduce the degeneracy between $\varepsilon^{uS}_{\alpha\beta}$ and $\varepsilon^{dS}_{\alpha\beta}$.

Finally, Fig. 7 displays the 90% C.L. allowed regions for the pairs of tensor couplings $\left(\varepsilon^{uT}_{e\mu}, \varepsilon^{dT}_{e\mu}\right)$ (left panel) and $\left(\varepsilon^{uT}_{\mu\tau}, \varepsilon^{dT}_{\mu\tau}\right)$ (right panel). Qualitatively similar features to the scalar case can be observed, except that CEνNS is much less sensitive to tensor couplings, and that the line slope has a different dependence on the proton to neutron ratio of the nucleus. This explains the shape of the NaI region, but the poor sensitivity of CEνNS to tensor GNI parameters makes it difficult to reduce the degeneracy between $\varepsilon^{uT}_{\alpha\beta}$ and $\varepsilon^{dT}_{\alpha\beta}$ with a NaI detector.

C. Impact of statistics, systematic uncertainties and background level

In the previous subsections, we argued that the ability of the future NaI detector to set better constraints on generalized neutrino interactions than the current CsI detector was limited by its low signal-over-background ratio. In order to support this statement, and to identify other limiting factors, we now study the impact of statistics, systematic uncertainties and background level on the expected sensitivity of the future NaI detector to GNI parameters. To this end, we consider three

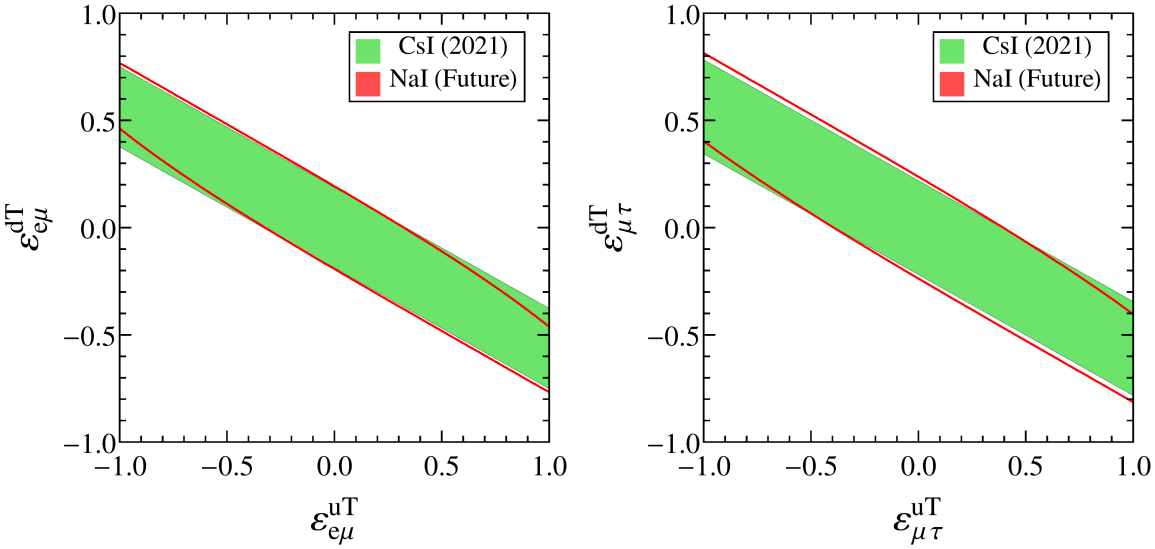

FIG. 7. Same as Fig. 6, but for the pairs of tensor GNI parameters $\left(\varepsilon^{uT}_{e\mu}, \varepsilon^{dT}_{e\mu}\right)$ (left panel) and $\left(\varepsilon^{uT}_{\mu\tau}, \varepsilon^{dT}_{\mu\tau}\right)$ (right panel).

scenarios characterized by more optimistic assumptions about the exposure time, signal systematic uncertainty or background control than the ones made in the previous subsections. In Scenario A, we assume five years of data taking with the same systematic errors as before (namely, $\sigma_{sig} = 10\%$ and $\sigma_{bg} = 5\%$). In Scenario B, we consider a running time of three years as in the previous subsections, but reduce the signal systematic uncertainty to $\sigma_{sig} = 5\%$, while keeping $\sigma_{bg} = 5\%$. Finally, in Scenario C, we assume a reduced background of 100 ckkd (to be compared with 400 ckkd in the first two recoil energy bins and 300 ckkd in the other bins in the previous subsections), with the same running time and systematic uncertainties as before.

Let us first discuss Scenario A. In Fig. 8, we show the expected sensitivity of the future NaI detector to some representative GNI parameters. In each panel, we compare the results of the previous subsections (red solid lines/red region) with the ones obtained with the larger statistics of Scenario A (blue dashed lines/blue contour). In the upper left panel, one can see that increasing the statistics makes it possible for the NaI detector to exclude the second minimum of the $\Delta\chi^2$ profile for the vector coupling $\varepsilon^{uV}_{\mu\mu}$ at the 2σ confidence level. Similarly, in the upper right panel, the larger statistics of Scenario A allows to further reduce the degeneracy between the vector couplings ε^{uV}_{ee} and $\varepsilon^{uV}_{\mu\mu}$, especially around $\left(\varepsilon^{uV}_{ee}, \varepsilon^{uV}_{\mu\mu}\right) \approx (-0.12, 0.2)$. This result illustrates the capability of a detector made of two nuclei with different proton to neutron ratios to lift degeneracies among NSI parameters, almost as efficiently as combinations of two different detectors, as discussed in Ref. [39] in the context of proposed experiments at the European Spallation Source. However, statistics

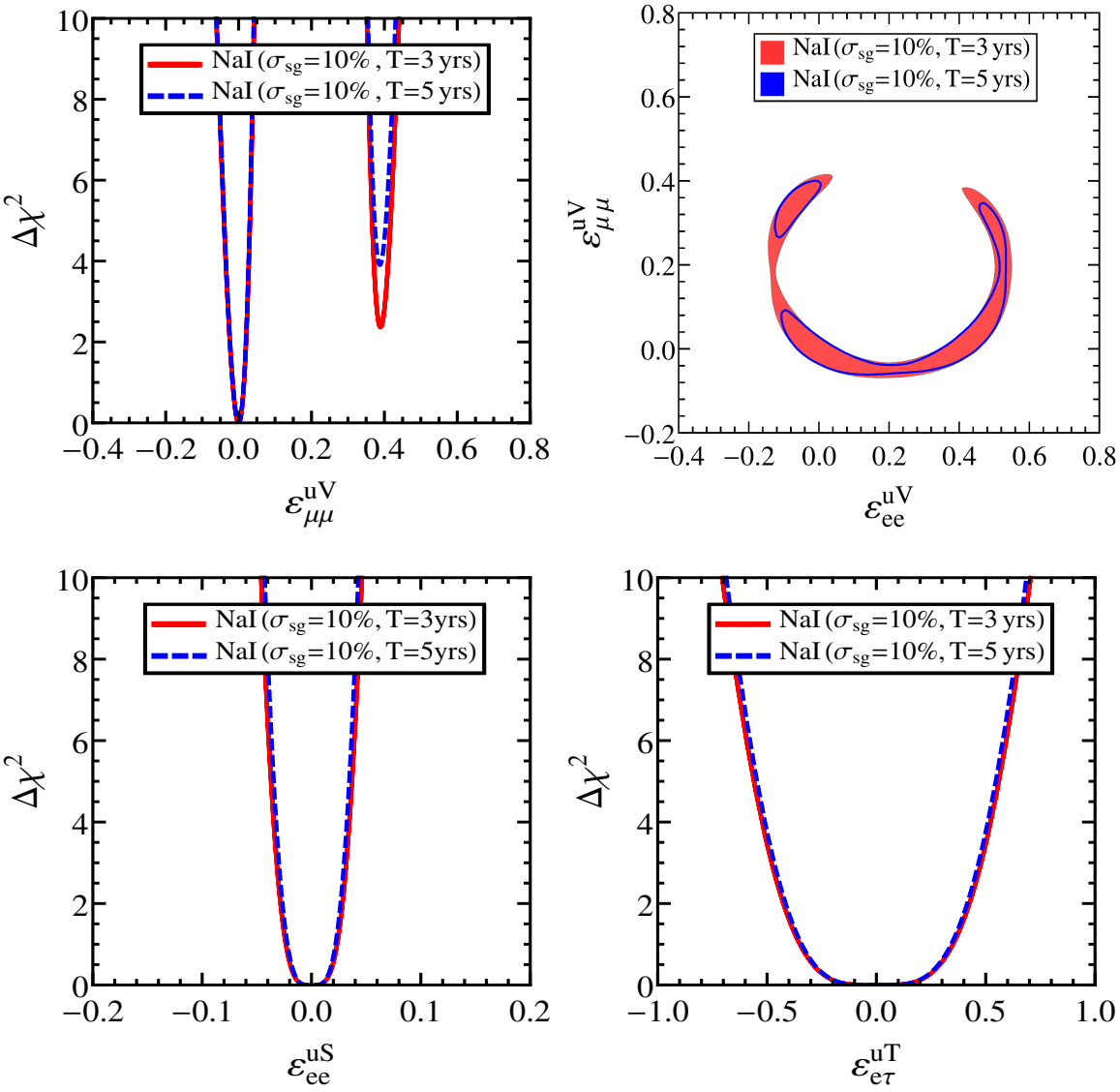

FIG. 8. Expected sensitivities of the future NaI detector to different GNI parameters, assuming 3 years (assumption of Subsections V A and V B, red solid lines/red region) or 5 years (Scenario B, blue dashed lines/blue contour) of data taking at the SNS. Upper left panel: one-dimensional $\Delta\chi^2$ profile for the vector coupling $\varepsilon^{uV}_{\mu\mu}$. Upper right panel: 90% C.L. allowed region for the pair of vector couplings (ε^{uV}_{ee}, $\varepsilon^{uV}_{\mu\mu}$). Lower panels: one-dimensional $\Delta\chi^2$ profiles for the scalar coupling ε^{uS}_{ee} (left) and tensor coupling $\varepsilon^{uT}_{e\tau}$ (right), both assumed to be real.

and (as we will see later) a good signal-over-background ratio are crucial to fully benefit from the presence of nuclei with different proton to neutron ratios in the same target material. Finally, the bottom panels of Fig. 8 show the $\Delta\chi^2$ profiles for the scalar coupling ε^{uS}_{ee} (left panel) and tensor coupling $\varepsilon^{uT}_{e\tau}$ (right panel). One can see that increasing the exposure time from 3 to 5 years does

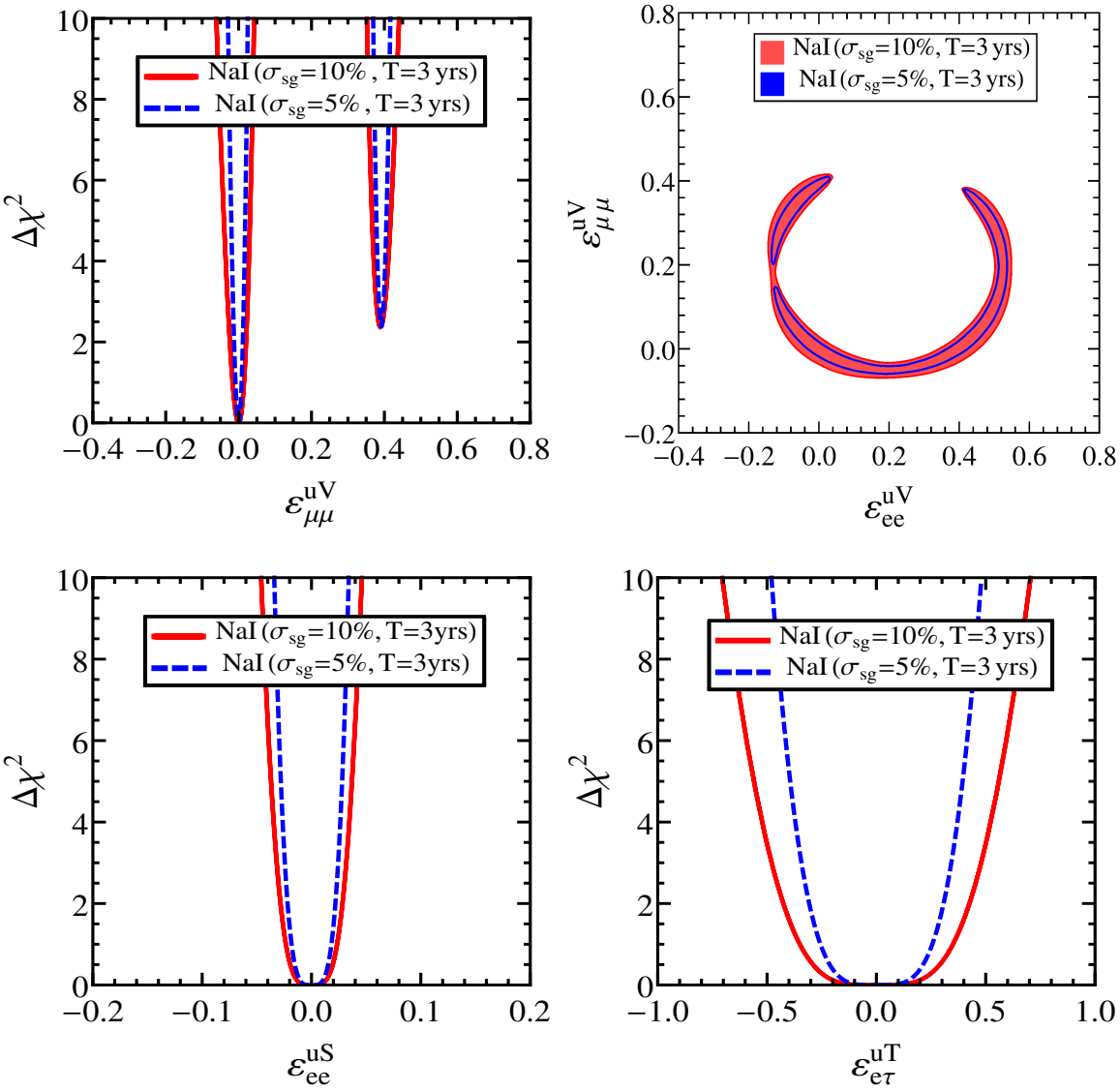

FIG. 9. Expected sensitivities of the future NaI detector to different GNI parameters, assuming a signal systematic uncertainty of 10% (assumption of Subsections V A and V B, red solid lines/red region) or 5% (Scenario B, blue dashed lines/blue contour). Upper left panel: one-dimensional $\Delta\chi^2$ profile for the vector coupling $\varepsilon^{uV}_{\mu\mu}$. Upper right panel: 90% C.L. allowed region for the pair of vector couplings (ε^{uV}_{ee}, $\varepsilon^{uV}_{\mu\mu}$). Lower panels: one-dimensional $\Delta\chi^2$ profiles for the scalar coupling ε^{uS}_{ee} (left) and tensor coupling $\varepsilon^{uT}_{e\tau}$ (right), both assumed to be real.

not result in a significant improvement of the expected sensitivity to those GNI parameters.

Let us now study the impact of the signal systematic uncertainty. In Fig. 9, we compare the results of the previous subsections (red solid lines/red region) with the ones obtained with the smaller σ_{sig} of Scenario B (blue dashed lines/blue contour), for the same GNI parameters as in Fig. 8. As can be seen, the main effect of reducing the signal systematic error is to improve the

sensitivity to GNI parameters, resulting in smaller allowed intervals or regions at a given confidence level. The impact on degeneracies is less important. In particular, the allowed region in the upper right panel is thinner for $\sigma_{sig} = 5\%$ than for $\sigma_{sig} = 10\%$ (which results in a partial breaking of the degeneray around $\left(\varepsilon_{ee}^{uV}, \varepsilon_{\mu\mu}^{uV}\right) \approx (-0.12, 0.2)$), but the region keeps roughly the same extent. Also, the second minimum of the $\Delta\chi^2$ profile for $\varepsilon_{\mu\mu}^{uV}$ (upper left panel) is excluded at the same confidence level for $\sigma_{sig} = 5\%$ and $\sigma_{sig} = 10\%$.

Finally, we consider Scenario C, which assumes a reduced background level of 100 ckkd in all recoil energy bins, as opposed to 400 ckkd in the first two bins and 300 ckkd in the other bins in Subsections V A and V B. In Fig. 10, we present the expected sensitivity of the future NaI detector to different GNI parameters, both in Scenario C and under the assumptions of Subsections V A and V B. The running time, signal and background systematic uncertainties are the same in both cases. As can be seen from the upper right panel (see also the lower left panel for a different type of degeneracy), a reduction of the background level by 66% (75% in the first two recoil energy bins) is more efficient at breaking degeneracies between NSI parameters than an increase of the running time from 3 to 5 years (Fig. 8), or a decrease of the signal systematic uncertainty by 50% (Fig. 9). The same statement holds for the second minimum of the $\Delta\chi^2$ profile for $\varepsilon_{\mu\mu}^{uV}$ (upper left panel), which is excluded at the 99% confidence level in Scenario C. In fact, such a level of background reduction would make the future NaI detector competitive with some of the best combinations of future advanced detectors at the European Spallation Source [39]. By contrast, the sensivity to tensor and scalar couplings of the NaI detector is only slightly ameliorated by a better background control (as illustrated in the right panel in the case of the parameter $\varepsilon_{e\tau}^{uT}$), while a reduction of the signal systematic error has a much stronger impact (see the lower panels of Fig. 9).

VI. CONCLUSIONS

In this work, we studied the potential of a NaI detector with characteristics similar to the one that is currently being deployed by the COHERENT collaboration to constrain scalar, vector, and tensor GNIs via CEνNS measurements at the Spallation Neutron Source. Compared with the current CsI detector, this new detector has the interesting property that its target material is composed of two nuclei with significantly different proton to neutron ratios, a feature that is known to help break degeneracies among NSI parameters. Furthermore, the future NaI detector benefits from a larger statistics than the current CsI detector, but suffers from a much less favorable signal-over-background ratio. As a consequence, the NaI detector is not expected to significantly improve

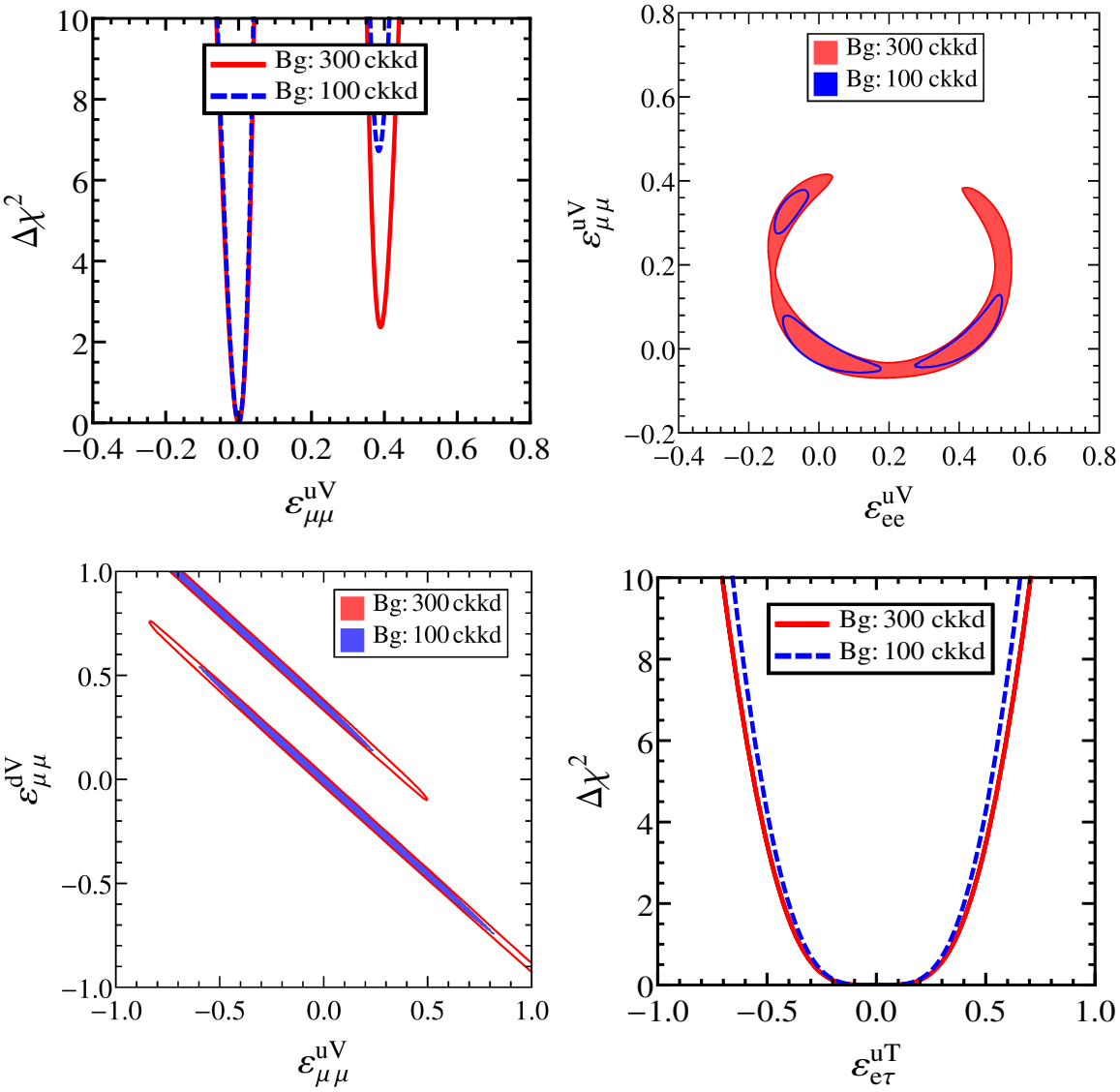

FIG. 10. Expected sensitivities of the future NaI detector to different GNI parameters, assuming the background level of Subsections V A and V B (red solid lines/red region) or 100 ckkd (Scenario C, blue dashed lines/blue contour). Upper left panel: one-dimensional $\Delta\chi^2$ profile for the vector coupling $\varepsilon^{uV}_{\mu\mu}$. Upper right panel: 90% C.L. allowed region for the pair of vector couplings $(\varepsilon^{uV}_{ee}, \varepsilon^{uV}_{\mu\mu})$. Lower left panel: 90% C.L. allowed region for the pair of vector couplings $(\varepsilon^{uV}_{\mu\mu}, \varepsilon^{dV}_{\mu\mu})$. Lower right panel: one-dimensional $\Delta\chi^2$ profile for the tensor coupling $\varepsilon^{uT}_{e\tau}$, assumed to be real.

the current CsI bounds on individual GNI parameters, except for diagonal vector couplings, whose contribution interfere with the Standard Model one in the CEνNS cross section. The NaI detector is also able to partially break degeneracies between two diagonal vector couplings, in a way that is complementary to the current CsI detector. These results are based on the technical details about

the NaI detector given in Refs. [53, 55] and on the background studies of Ref. [53], as well as on our assumptions about signal and background systematic uncertainties.

We also studied the impact of statistics, signal systematic uncertainty and background level on the expected sensitivity of the future NaI detector to GNIs. We found that reducing the signal systematic uncertainty from 10% to 5% significantly improves the sensitivity to all GNI parameters, while increasing the running time from three to five years makes it possible to further break degeneracies among diagonal NSIs, but has little impact on the sensitivity to GNI parameters whose contribution to CEνNS does not interfere with the SM contribution. Our results also show that a good background control is crucial to fully benefit from the different proton to neutron ratios of the Sodium and Iodine targets. More specifically, a background level of 100 counts per keV$_{ee}$ per kg per day (ckkd), if achievable, would make the NaI detector considered in this work very efficient at breaking degeneracies among NSI parameters, already after three years of data taking.

ACKNOWLEDGMENTS

The work of S.S.C. is funded by the Deutsche Forschungsgemeinschaft (DFG, German Research Foundation) – project number 510963981. S. S. C. also acknowledges financial support from the LabEx P2IO (ANR-10-LABX-0038 - Project "BSMNu") in the framework of the "Investissements d'Avenir" (ANR-11-IDEX-0003-01) managed by the Agence Nationale de la Recherche (ANR), France. This work has been supported by the Spanish grants PID2020-113775GB-I00 (MCIN/AEI/10.13039/501100011033) and CIPROM/2021/054 (Generalitat Valenciana). G.S.G. acknowledges financial support by the CIAPOS/2022/254 grant funded by Generalitat Valenciana. The work of SL is supported in part by the European Union's Horizon 2020 research and innovation programme under the Marie Sklodowska-Curie grant agreement No. 860881-HIDDeN. O. G. M. was supported by the CONAHCyT grant 23238 and by SNII-Mexico.

[1] D. Z. Freedman, "Coherent effects of a weak neutral current," Phys. Rev. D **9** (Mar, 1974) 1389–1392. https://link.aps.org/doi/10.1103/PhysRevD.9.1389.

[2] **COHERENT** Collaboration, D. Akimov et al., "Observation of Coherent Elastic Neutrino-Nucleus Scattering," Science **357** no. 6356, (2017) 1123–1126, arXiv:1708.01294 [nucl-ex].

[3] D. Akimov et al., "Measurement of the Coherent Elastic Neutrino-Nucleus Scattering Cross Section on CsI by COHERENT," arXiv:2110.07730 [hep-ex].

[4] **COHERENT** Collaboration, D. Akimov et al., "First Measurement of Coherent Elastic Neutrino-Nucleus Scattering on Argon," Phys. Rev. Lett. **126** no. 1, (2021) 012002, arXiv:2003.10630 [nucl-ex].

[5] M. Cadeddu, N. Cargioli, F. Dordei, C. Giunti, Y. F. Li, E. Picciau, C. A. Ternes, and Y. Y. Zhang, "New insights into nuclear physics and weak mixing angle using electroweak probes," Phys. Rev. C **104** no. 6, (2021) 065502, arXiv:2102.06153 [hep-ph].

[6] M. Cadeddu, C. Giunti, Y. Li, and Y. Zhang, "Average CsI neutron density distribution from COHERENT data," Phys. Rev. Lett. **120** no. 7, (2018) 072501, arXiv:1710.02730 [hep-ph].

[7] O. Miranda, D. Papoulias, G. Sanchez Garcia, O. Sanders, M. Tórtola, and J. Valle, "Implications of the first detection of coherent elastic neutrino-nucleus scattering (CEvNS) with Liquid Argon," JHEP **05** (2020) 130, arXiv:2003.12050 [hep-ph].

[8] J. Barranco, O. G. Miranda, and T. I. Rashba, "Probing new physics with coherent neutrino scattering off nuclei," JHEP **12** (2005) 021, arXiv:hep-ph/0508299.

[9] K. Scholberg, "Prospects for measuring coherent neutrino-nucleus elastic scattering at a stopped-pion neutrino source," Phys. Rev. D **73** (2006) 033005, arXiv:hep-ex/0511042.

[10] V. De Romeri, O. G. Miranda, D. K. Papoulias, G. Sanchez Garcia, M. Tórtola, and J. W. F. Valle, "Physics implications of a combined analysis of COHERENT CsI and LAr data," JHEP **04** (2023) 035, arXiv:2211.11905 [hep-ph].

[11] V. Bresó-Pla, A. Falkowski, M. González-Alonso, and K. Monsálvez-Pozo, "EFT analysis of New Physics at COHERENT," JHEP **05** (2023) 074, arXiv:2301.07036 [hep-ph].

[12] D. Aristizabal Sierra, V. De Romeri, and N. Rojas, "COHERENT analysis of neutrino generalized interactions," Phys. Rev. D **98** (2018) 075018, arXiv:1806.07424 [hep-ph].

[13] L. J. Flores, N. Nath, and E. Peinado, "Non-standard neutrino interactions in U(1)' model after COHERENT data," JHEP **06** (2020) 045, arXiv:2002.12342 [hep-ph].

[14] T. Han, J. Liao, H. Liu, and D. Marfatia, "Scalar and tensor neutrino interactions," JHEP **07** (2020) 207, arXiv:2004.13869 [hep-ph].

[15] M. Cadeddu, F. Dordei, C. Giunti, Y. F. Li, and Y. Y. Zhang, "Neutrino, electroweak, and nuclear physics from COHERENT elastic neutrino-nucleus scattering with refined quenching factor," Phys. Rev. D **101** no. 3, (2020) 033004, arXiv:1908.06045 [hep-ph].

[16] O. G. Miranda, D. K. Papoulias, M. Tórtola, and J. W. F. Valle, "Probing neutrino transition magnetic moments with coherent elastic neutrino-nucleus scattering," JHEP **07** (2019) 103, arXiv:1905.03750 [hep-ph].

[17] M. Cadeddu, F. Dordei, C. Giunti, Y. F. Li, E. Picciau, and Y. Y. Zhang, "Physics results from the first COHERENT observation of coherent elastic neutrino-nucleus scattering in argon and their combination with cesium-iodide data," Phys. Rev. D **102** no. 1, (2020) 015030, arXiv:2005.01645 [hep-ph].

[18] Y. Farzan, M. Lindner, W. Rodejohann, and X.-J. Xu, "Probing neutrino coupling to a light scalar with coherent neutrino scattering," JHEP **05** (2018) 066, arXiv:1802.05171 [hep-ph].

[19] L. M. G. de la Vega, L. J. Flores, N. Nath, and E. Peinado, "Complementarity between dark matter direct searches and CEνNS experiments in U(1)' models," JHEP **09** (2021) 146, arXiv:2107.04037 [hep-ph].

[20] E. Bertuzzo, G. Grilli di Cortona, and L. M. D. Ramos, "Probing light vector mediators with coherent scattering at future facilities," JHEP **06** (2022) 075, arXiv:2112.04020 [hep-ph].

[21] B. Dutta, Y. Gao, R. Mahapatra, N. Mirabolfathi, L. E. Strigari, and J. W. Walker, "Sensitivity to oscillation with a sterile fourth generation neutrino from ultra-low threshold neutrino-nucleus coherent scattering," Phys. Rev. D **94** no. 9, (2016) 093002, arXiv:1511.02834 [hep-ph].

[22] T. S. Kosmas, D. K. Papoulias, M. Tortola, and J. W. F. Valle, "Probing light sterile neutrino signatures at reactor and Spallation Neutron Source neutrino experiments," Phys. Rev. D **96** no. 6, (2017) 063013, arXiv:1703.00054 [hep-ph].

[23] D. Akimov et al., "The COHERENT Experimental Program," in Snowmass 2021. 4, 2022. arXiv:2204.04575 [hep-ex].

[24] D. Baxter et al., "Coherent Elastic Neutrino-Nucleus Scattering at the European Spallation Source," JHEP **02** (2020) 123, arXiv:1911.00762 [physics.ins-det].

[25] **CCM** Collaboration, A. A. Aguilar-Arevalo et al., "First Dark Matter Search Results From Coherent CAPTAIN-Mills," arXiv:2105.14020 [hep-ex].

[26] **CONUS** Collaboration, H. Bonet et al., "Novel constraints on neutrino physics beyond the standard model from the CONUS experiment," JHEP **05** (2022) 085, arXiv:2110.02174 [hep-ph].

[27] **CONNIE** Collaboration, A. Aguilar-Arevalo et al., "Results of the Engineering Run of the Coherent Neutrino Nucleus Interaction Experiment (CONNIE)," JINST **11** no. 07, (2016) P07024, arXiv:1604.01343 [physics.ins-det].

[28] **νGeN** Collaboration, I. Alekseev et al., "First results of the νGeN experiment on coherent elastic neutrino-nucleus scattering," Phys. Rev. D **106** no. 5, (2022) L051101, arXiv:2205.04305 [nucl-ex].

[29] D. Y. Akimov, I. Alexandrov, R. Alyev, V. Belov, A. Bolozdynya, A. Etenko, A. Galavanov, E. Glagovsky, Y. Gusakov, A. Khromov, et al., "The red-100 experiment," Journal of Instrumentation **17** no. 11, (2022) T11011.

[30] B. C. Canas, E. A. Garces, O. G. Miranda, A. Parada, and G. Sanchez Garcia, "Interplay between nonstandard and nuclear constraints in coherent elastic neutrino-nucleus scattering experiments," Phys. Rev. D **101** no. 3, (2020) 035012, arXiv:1911.09831 [hep-ph].

[31] R. R. Rossi, G. Sanchez Garcia, and M. Tórtola, "Probing nuclear properties and neutrino physics with current and future CEνNS experiments," arXiv:2311.17168 [hep-ph].

[32] M. Lindner, W. Rodejohann, and X.-J. Xu, "Coherent Neutrino-Nucleus Scattering and new Neutrino Interactions," JHEP **03** (2017) 097, arXiv:1612.04150 [hep-ph].

[33] T. Ohlsson, "Status of non-standard neutrino interactions," Rept. Prog. Phys. **76** (2013) 044201, arXiv:1209.2710 [hep-ph].

[34] O. G. Miranda and H. Nunokawa, "Non standard neutrino interactions: current status and future prospects," New J. Phys. **17** no. 9, (2015) 095002, arXiv:1505.06254 [hep-ph].

[35] Y. Farzan and M. Tortola, "Neutrino oscillations and Non-Standard Interactions," Front. in Phys. **6** (2018) 10, arXiv:1710.09360 [hep-ph].

[36] O. G. Miranda, M. A. Tortola, and J. W. F. Valle, "Are solar neutrino oscillations robust?," JHEP **10** (2006) 008, arXiv:hep-ph/0406280.

[37] P. Coloma and T. Schwetz, "Generalized mass ordering degeneracy in neutrino oscillation experiments," Phys. Rev. D **94** no. 5, (2016) 055005, arXiv:1604.05772 [hep-ph]. [Erratum: Phys.Rev.D 95, 079903 (2017)].

[38] A. Galindo-Uribarri, O. G. Miranda, and G. S. Garcia, "Novel approach for the study of coherent elastic neutrino-nucleus scattering," Phys. Rev. D **105** no. 3, (2022) 033001, arXiv:2011.10230 [hep-ph].

[39] S. S. Chatterjee, S. Lavignac, O. G. Miranda, and G. Sanchez Garcia, "Constraining nonstandard interactions with coherent elastic neutrino-nucleus scattering at the European Spallation Source," Phys. Rev. D **107** no. 5, (2023) 055019, arXiv:2208.11771 [hep-ph].

[40] O. Tomalak, P. Machado, V. Pandey, and R. Plestid, "Flavor-dependent radiative corrections in coherent elastic neutrino-nucleus scattering," JHEP **02** (2021) 097, arXiv:2011.05960 [hep-ph].

[41] J. D. Lewin and P. F. Smith, "Review of mathematics, numerical factors, and corrections for dark matter experiments based on elastic nuclear recoil," Astropart. Phys. **6** (1996) 87–112.

[42] J. Erler and R. Ferro-Hernández, "Weak Mixing Angle in the Thomson Limit," JHEP **03** (2018) 196, arXiv:1712.09146 [hep-ph].

[43] **Particle Data Group** Collaboration, R. L. Workman et al., "Review of Particle Physics," PTEP **2022** (2022) 083C01.

[44] S. R. Klein and J. Nystrand, "Exclusive vector meson production in relativistic heavy ion collisions," Phys. Rev. C **60** (Jun, 1999) 014903. https://link.aps.org/doi/10.1103/PhysRevC.60.014903.

[45] C. Giunti, "General COHERENT constraints on neutrino nonstandard interactions," Phys. Rev. D **101** no. 3, (2020) 035039, arXiv:1909.00466 [hep-ph].

[46] O. G. Miranda, G. Sanchez Garcia, and O. Sanders, "Coherent elastic neutrino-nucleus scattering as a precision test for the Standard Model and beyond: the COHERENT proposal case," Adv. High Energy Phys. **2019** (2019) 3902819, arXiv:1902.09036 [hep-ph].

[47] E. E. Jenkins, A. V. Manohar, and P. Stoffer, "Low-Energy Effective Field Theory below the Electroweak Scale: Operators and Matching," JHEP **03** (2018) 016, arXiv:1709.04486 [hep-ph].

[48] I. Bischer and W. Rodejohann, "General Neutrino Interactions at the DUNE Near Detector," Phys. Rev. D **99** no. 3, (2019) 036006, arXiv:1810.02220 [hep-ph].

[49] M. Hoferichter, J. Ruiz de Elvira, B. Kubis, and U.-G. Meißner, "High-Precision Determination of the Pion-Nucleon σ Term from Roy-Steiner Equations," Phys. Rev. Lett. **115** (2015) 092301, arXiv:1506.04142 [hep-ph].

[50] T. Bhattacharya, V. Cirigliano, S. Cohen, R. Gupta, H.-W. Lin, and B. Yoon, "Axial, Scalar and Tensor Charges of the Nucleon from 2+1+1-flavor Lattice QCD," Phys. Rev. D **94** no. 5, (2016) 054508, arXiv:1606.07049 [hep-lat].

[51] L. J. Flores, N. Nath, and E. Peinado, "CEνNS as a probe of flavored generalized neutrino interactions," Phys. Rev. D **105** no. 5, (2022) 055010, arXiv:2112.05103 [hep-ph].

[52] A. Majumdar, D. K. Papoulias, R. Srivastava, and J. W. F. Valle, "Physics implications of recent Dresden-II reactor data," Phys. Rev. D **106** no. 9, (2022) 093010, arXiv:2208.13262 [hep-ph].

[53] S. C. Hedges, Low Energy Neutrino-Nucleus Interactions at the Spallation Neutron Source. PhD thesis, Duke U., 2021 (https://hdl.handle.net/10161/24413).

[54] E. Picciau, Low-energy signatures in DarkSide-50 experiment and neutrino scattering processes. PhD thesis, Cagliari U., 2022.

[55] S. C. Hedges, "The NaI[Tl] COHERENT Detector,". Talk at the Magnificent CEνNS Workshop 2018 (doi:10.5281/zenodo.3462345).